Title

Teleseismic attenuation, temperature, and melt of the upper mantle in the Alaska subduction zone

Authors

Soto Castaneda, Roque A
Abers, Geoffrey A
Eilon, Zachary C
et al.

Publication Date

2021-01-16

DOI

10.1002/essoar.10505839.1

JGR Solid Earth

RESEARCH ARTICLE
10.1029/2021JB021653

Teleseismic Attenuation, Temperature, and Melt of the Upper Mantle in the Alaska Subduction Zone

R. A. Soto Castaneda[1], G. A. Abers[1], Z. C. Eilon[2], and D. H. Christensen[3]

[1]Department of Earth and Atmospheric Sciences, Cornell University, Ithaca, NY, USA, [2]Department of Earth Science, University of California, Santa Barbara, CA, USA, [3]Geophysical Institute, University of Alaska Fairbanks, Fairbanks, AK, USA

Key Points:

- Body-wave attenuation measurements reveal upper mantle structure, including subducting plates and the Alaskan sub-/back-arc
- The Wrangell Volcanic Field is underlain by Yakutat subduction, but geometry is complex
- Sedimentary basins unexpectedly produce negative apparent attenuation in body-wave spectra

Supporting Information:

Supporting Information may be found in the online version of this article.

Correspondence to:

G. A. Abers,
abers@cornell.edu

Citation:

Soto Castaneda, R. A., Abers, G. A., Eilon, Z. C., & Christensen, D. H. (2021). Teleseismic attenuation, temperature, and melt of the upper mantle in the Alaska subduction zone. *Journal of Geophysical Research: Solid Earth*, *126*, e2021JB021653. https://doi.org/10.1029/2021JB021653

Received 4 JAN 2021
Accepted 14 JUN 2021

Abstract Seismic deployments in the Alaska subduction zone provide dense sampling of the seismic wavefield that constrains thermal structure and subduction geometry. We measure *P* and *S* attenuation from pairwise amplitude and phase spectral ratios for teleseismic body waves at 206 stations from regional and short-term arrays. Parallel teleseismic travel-time measurements provide information on seismic velocities at the same scale. These data show consistently low attenuation over the forearc of subduction systems and high attenuation over the arc and backarc, similar to local-earthquake attenuation studies but at 10× lower frequencies. The pattern is seen both across the area of normal Pacific subduction in Cook Inlet, and across the Wrangell Volcanic Field where subduction has been debated. These observations confirm subduction-dominated thermal regime beneath the latter. Travel times show evidence for subducting lithosphere much deeper than seismicity, while attenuation measurements appear mostly reflective of mantle temperature less than 150 km deep, depths where the mantle is closest to its solidus and where subduction-related melting may take place. Travel times show strong delays over thick sedimentary basins. Attenuation signals show no evidence of absorption by basins, although some basins show signals anomalously rich in high-frequency energy, with consequent negative apparent attenuation. Outside of basins, these data are consistent with mantle attenuation in the upper 220 km that is quantitatively similar to observations from surface waves and local-earthquake body waves. Differences between *P* and *S* attenuation suggest primarily shear-modulus relaxation. Overall the attenuation measurements show consistent, coherent subduction-related structure, complementary to travel times.

Plain Language Summary Seismic waves lose more energy passing through hot and partly molten volumes than cold regions. As a result, measurements of variation in their amplitudes, or attenuation, provides a tool for mapping out the upper mantle, complementing more traditional measurements of their variation in travel time. New high-quality arrays across southern Alaska, along with recent methodological developments, now allow this measurement to be made systematically across the entire region. They show consistently low attenuation where subducting plates are near the surface or along paths that follow the cold subducting plates. These regions are in southernmost Alaska. By contrast, signals traveling beneath volcanic regions or north of them, where hot mantle flows toward subduction zones, show high attenuation. The attenuation patterns resemble those from travel time, but seem to show more sensitivity to the upper 150 km of the Earth while travel time delays more uniformly sample deeper. Sedimentary basins show confusing signals, with travel time delays as expected for low-wavespeed sediments, but high amplitudes that are difficult to explain. These signals allow quantitative mapping of temperature and melt variations in the upper mantle, even in regions as complex as subduction zones where both properties vary rapidly over short distances.

1. Introduction

Seismic imaging offers critical insight into mantle thermal structure and melting in subduction zones. While seismic velocities provide first-order constraints, alone they suffer from ambiguities in resolving melt from temperature (e.g., Hammond & Humphreys, 2000) and are sensitive to composition and crustal geology. Seismic attenuation (parameterized by its reciprocal, the quality factor *Q*) can provide powerful constraints with greater sensitivity to temperature, potentially to melt, and relatively less to composition than velocity measurements (Dalton et al., 2009; Faul & Jackson, 2005; Karato, 2003; Takei, 2017). In subduction zones, high attenuation (low *Q*) beneath volcanic arcs exceeds that predicted by temperature alone and

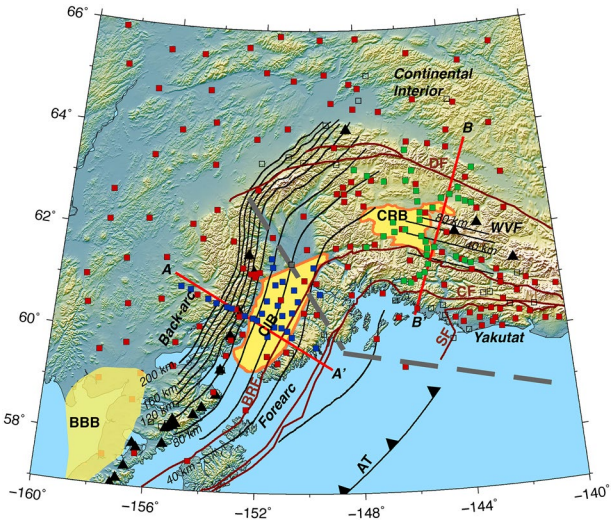

Figure 1. Alaska study region and major features. Black lines: Wadati-Benioff zone contours at 20 km intervals; dark red lines: major terrane-bounding faults; yellow areas: Cook Inlet (CIB), Copper River (CRB) and Bristol Bay (BBB) basins; gray dashed line: inferred west edge of Yakutat terrane; black triangles: Quaternary volcanoes. Squares are seismometers examined in this study, filled if used in final results and open if not, blue are SALMON and green are WVLF short-term deployments while red are other stations. Red lines A-A' and B-B' show transects across Cook Inlet and WVF respectively. Other abbreviations: WVF, Wrangell Volcanic Field; DF, Denali Fault; CF, Contact Fault; BRF, Border Ranges Fault.

likely indicates some in situ melt (Abers et al., 2014). That observation contrasts strongly with the negligible attenuation seen within subducting plates and shallow forearcs where temperatures are expected to be very low (e.g., Pozgay et al., 2009; Roth et al., 1999; Stachnik et al., 2004; Wei & Wiens, 2018). However, such observations are limited because they rely on signals from earthquakes within the Wadati-Benioff Zone (WBZ) directly beneath seismometers, so are available only directly above regions of abundant WBZ seismicity. Recent developments in the use of teleseismic waveforms, used here, avoid this limitation and provide potentially comparable resolution for teleseismic velocity and attenuation studies (Eilon & Abers, 2017).

South central Alaska provides a relatively accessible, modern example of the complexities present where subduction systems terminate along strike. The largely amagmatic, east end of the Aleutian subduction system gives way to the Wrangell Volcanic Field (WVF) just north of the Yakutat collision (e.g., Plafker & Berg, 1994). The relationship between the WVF and subduction remains controversial (e.g., Jiang et al., 2018; Martin-Short et al., 2016, 2018). The expansion of the EarthScope Transportable Array (TA) to south central Alaska beginning in 2014 has provided some of the first seismic imaging of the region at moderate resolution, and here we augment that data set with observations from two focused high-resolution broadband seismic deployments, WVLF (Wrangell Volcanism and Lithospheric Fate; Christensen & Abers, 2016) and SALMON (Tape et al., 2017). We extract information about both seismic attenuation and seismic velocities from teleseismic body waves (Eilon & Abers, 2017), in an attempt to untangle the effects of composition, temperature, melt, and near-surface effects. The data show clear signatures of subduction and the hot mantle wedge beneath both the eastern Aleutian arc and the WVF.

1.1. Tectonic Setting

South-Central Alaska (Figure 1) was formed by a series of collisions of exotic terranes, culminating in the Cenozoic collision of the Yakutat terrane into the North American continent (Plafker & Berg, 1994; Trop & Ridgway, 2007). The Yakutat terrane is likely an oceanic plateau currently converging with south-central Alaska (e.g., Bruns, 1983; Christeson et al., 2010; Worthington et al., 2012). Its 15–25 km thick crust has been imaged subducting to at least 140 km depth beneath the Alaska Range west of 147°W, where intermediate-depth seismicity is abundant (Eberhart-Phillips et al., 2006; Ferris et al., 2003). To the east, its fate is more ambiguous; at shallow depths the Yakutat block actively underthrusts coastal Alaska (Elliott & Freymueller, 2020; Pavlis et al., 2004), but it is unclear whether Yakutat lithosphere subducts coherently or collides. The Yakutat basin overlies the Yakutat terrane and comprises various Cenozoic sedimentary strata reaching 10 km in thickness (Trop & Ridgway 2007).

The subduction of the Pacific Plate beneath the 3,000 km long Aleutian island arc causes extensive arc volcanism as far east as Cook Inlet (Buurman et al., 2014). Although WBZ seismicity continues another 350 km farther east, volcanism is absent with the exception of a small Quaternary maar roughly overlying the east end of intermediate-depth seismicity (Nye et al., 2018; Plafker & Berg, 1994). The WVF contains several active volcanoes younger than 25 Ma (Richter et al., 1990) with generally calc-alkaline, arc-like eruptive products, with some exceptions (Preece & Hart, 2004); the presence of adakitic ashes and lavas potentially indicates slab-edge-type melting (Brueske et al., 2019). Some recent tomographic analyses of seismic surface and body waves indicate a high velocity anomaly extending 85–100 km past the edge of the WBZ at 147°W (Jiang et al., 2018; Wang & Tape, 2014; Ward, 2015), although other studies do not (Berg et al., 2020; Martin-Short et al., 2018). The same studies also disagree over the extent and existence of the slab beneath the WVF.

2. Data

We examine data from broadband seismometers between 55° and 65°N and 160° to 140°W collected between 2015 and 2017 from both portable and long-term arrays in the region (Figure 1). Data come from the Earthscope Transportable Array and permanent regional networks (Ruppert & West, 2020) as well as two dense short-term arrays, WVLF and SALMON. The WVLF array featured 35 broadband seismometers deployed from June 2016 to June 2018 in the Central Alaska subduction zone and WVF regions (McPherson et al., 2020); this study only analyzes the first year of recording. The SALMON array includes 28 broadband, direct-burial posthole seismometers spanning the Cook Inlet region of the Alaska Subduction zone from summer 2015 to summer 2017 (Tape et al., 2017).

The primary signals are teleseismic (30°–90° distance) *P* and *S* waveforms, measured on vertical and transverse components, respectively, these signals are suitable for both cross-correlation for travel times and frequency-dependent analysis for attenuation as described below. Usable data were obtained for 167 teleseisms with $M_W \geq 6.0$ from June 2015 through July 2017, recorded across 206 unique stations. Three-component seismic waveforms were down-sampled to 10 samples per second to achieve a parity in the sampling rate for data from different arrays, and the instrument response was removed. Waveforms were windowed 40 s before and after the predicted arrival and then extended 20% prior to applying a 20% Tukey window.

Core-phase interference (*SKS*) can complicate *S* waves, so we tested a maximum epicentral distance cutoff of 70° for *S*. The cutoff diminished the pool of available events from 167 to 32 and resulted in poor azimuthal coverage, but showed no systematic changes to results, so our final analysis used events from the full 30°-90° range. Our use of the transverse component isolates the SH component of the *S* waves, minimizing the impact of *SKS* energy within this window as well as other P-S mode-converted signals, which are to first order radially polarized. Notwithstanding, signals that have visible overlap of *SKS* and *S* within the spectral calculation window (described below) on more than half of the recorded traces are manually discarded. After this and other quality control described below, 89 earthquakes were used for both *S* and *P* phases.

3. Methods

The primary measurements were differential travel times (ΔT) and differential integrated attenuation values (Δt^*) for each usable station—event pair. The methods and workflow are described elsewhere (Eilon & Abers, 2017; Soto Castaneda, 2020) and summarized here. The station-specific ΔT and Δt^* were derived from differential measurements between each pair of stations for every event. Different subsets of events were recorded by each individual station, and each individual event was recorded at different subsets of stations, so simple station averages would not yield consistent values. We therefore jointly inverted all pairwise data as described below, treating velocity or attenuation from *P* or *S* signals as four separate inversions, to solve for event terms and single values of ΔT or Δt^* for each station.

3.1. Differential Travel Times

To calculate the ΔT, waveforms were cross-correlated after applying a bandpass filter of 0.083–1 Hz and from 0.2 to 1 Hz for the *S* and *P* waveforms respectively, within a hand-picked window of 10–20 s duration around the first arrival. We discarded waveform pairs with cross-correlation coefficients of less than 0.65. The remaining traces were used to compute single-station travel time residuals, ΔT, following standard methods (VanDecar & Crosson, 1990). These station residuals were then applied to align waveforms for attenuation measurements. This procedure resulted in 8,061 ΔT_P and 7,565 ΔT_S measurements.

3.2. Attenuation

Differential attenuation Δt^* was derived from spectral ratios of station pairs. After deconvolving instrument response, the differences in signal between stations are attributed to differential attenuation between paths to the two stations. These measurements are described by a differential attenuation operator

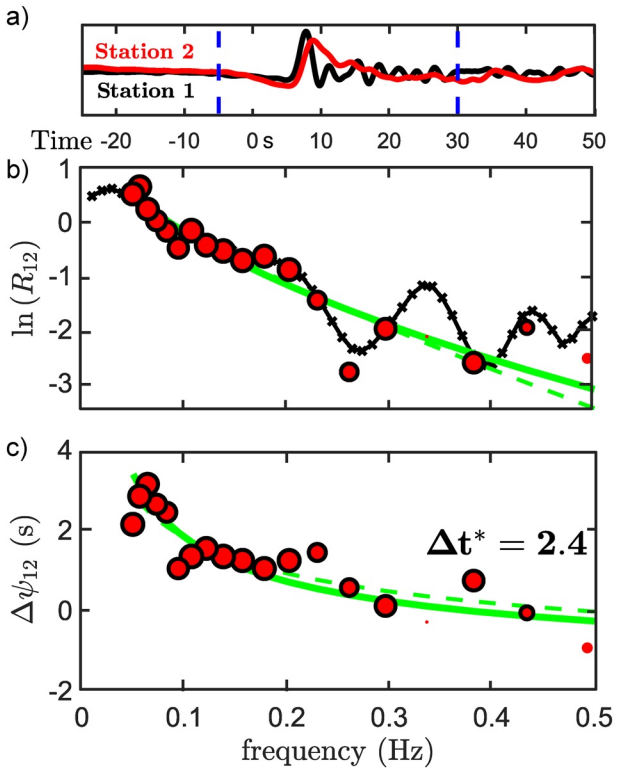

Figure 2. (a) Example of *S*-wave differential attenuation measurement between two stations, CUT (Chulitna, Alaska; black) and RED (Mount Redoubt, Alaska; red). Blue lines indicate windows for spectra calculation. (b) Logarithm of amplitude ratios. (c) Differential phase. In (b) and (c), red circles are measurements at each narrow band filter; size reflects robustness of measurement of each narrow band as measured by maximum cross-correlation. Solid green line: best fit assuming no frequency dependence of attenuation; dashed green line best fit assuming frequency dependence coefficient of 0.27. Black line in (b) is the spectral ratio calculated by spectral division.

$$\Delta t^*_{ij} = \Delta t^*_i - \Delta t^*_j \tag{1}$$

as the difference between Δt^* recorded at station i and j (e.g., Roth et al., 1999). In amplitude and phase the spectral ratios are related to this operator as:

$$\ln\left(R_{ij}\left(f\right)\right) = k_{1ij} - \pi f \Delta t^*_{ij}, \tag{2}$$

$$\Delta\varphi_{ij}\left(f\right) = k_{2ij} + \frac{1}{\pi}\ln\left(\frac{f}{f_0}\right)\Delta t^*_{ij}, \tag{3}$$

where $R_{ij}\left(f\right)$ is the spectral amplitude ratio between stations i and j, $\Delta\varphi_{ij}\left(f\right)$ is the spectral phase shift, k_{1ij} describes a frequency-independent differential amplification between stations, k_{2ij} represents a frequency-independent phase shifts (Eilon & Abers, 2017), and f_0 is the reference frequency (chosen to be 1 Hz). Each pairwise measurement of amplitude ratio R_{ij} and differential phase $\Delta\varphi_{ij}$ over a range of frequency f provides a constraint on the corresponding differential attenuation operator Δt^*_{ij}.

We test for frequency dependence of attenuation of the form $t^*\left(f\right) = t^*_0 f^{-\alpha}$ typical of many descriptions and laboratory measurements (e.g., Faul & Jackson, 2005), where t^*_0 is the integrated attenuation at the reference frequency. The expressions in Equations 2 and 3 are appropriate for frequency independent ($\alpha = 0$) attenuation (e.g., Faul & Jackson, 2005; Stachnik et al., 2004). Following several studies that show weak frequency dependence of $\alpha = 0.27$, we also test this case, leading to a modification of the expressions (e.g., Anderson & Minster, 1979; Eilon & Abers, 2017):

$$\ln\left(R_{ij}\left(f\right)\right) = k_{1ij} - \pi f_0^{\alpha} f^{1-\alpha} \Delta t^*_{0ij}, \tag{4}$$

$$\Delta\varphi_{ij}\left(f\right) = k_{2ij} + \frac{1}{2}\cot\left(\frac{\alpha\pi}{2}\right) f_0^{\alpha} f^{-\alpha} \Delta t^*_{0ij}. \tag{5}$$

3.3. Measurements of Amplitude, Phase and Δt^*

Amplitude ratios and phase differences between stations recording the same earthquake are measured at a range of narrow frequency bands, through a multiple-narrowband-filter technique (Dziewonski et al., 1969). This filter-bank method has been demonstrated to improve upon Fourier-domain amplitude spectral ratio methods by increasing the range of useable frequencies and through the inclusion of phase data (Bezada et al., 2019; Soto Castaneda, 2020). For a 35 s window starting 5 s before the first arrival, each trace is run through a comb of 30 narrow-band filters logarithmically spaced in center frequency from 0.05 to 0.5 Hz (Eilon, 2016). At each frequency for which the signal exceeds noise, the $\Delta\varphi_{ij}$ and R_{ij} for each station pair are measured by time-shifting and amplitude-scaling signals in the time domain from these narrow-band-filtered waveforms (e.g., Figure 2). The squared correlation-coefficient between shifted and scaled waveforms at each individual frequency is used as weights $w_{ij}(f)$ in the subsequent inversion for Δt^*, ensuring that we only compare portions of the spectra for which the two waveforms are compatible. Only measurements for which correlation coefficients exceed 0.5 are retained. We discard any station pair for which fewer than four frequencies have signal that exceeds 10 times the pre-event noise, and any trace for which the cross-correlation coefficient with the stacked trace for that event is less than 0.5.

For each phase, station-specific Δt^*_i values are determined by minimizing

$$E = A \sum_{ijm} w_{ijm} \left(\ln\left(R_{ijm}^{obs}\right) - \ln\left(R_{ijm}\right) \right)^2 + \sum_{ijm} w_{ijm} \left(\Delta\varphi_{ijm}^{obs} - \Delta\varphi_{ijm} \right)^2 \quad (6)$$

combining Equation 1 with either Equations 2 and 3 or Equations 4 and 5, where R_{ijm} is the predicted amplitude ratio from Equation 2 or Equation 4 at the m^{th} frequency, $\Delta\varphi_{ijm}$ is the corresponding phase ratio, R_{ijm}^{obs} and $\Delta\varphi_{ijm}^{obs}$ are their respective observations, w_{ijm} is as above, and A is a factor controlling the relative weighting of amplitude to phase misfit. After several trials, A is set to 2.0 in results presented here. This error function is minimized over all frequencies that meet the signal-to-noise criterion, solving for station-specific Δt_i^* via linear least-squares inversion.

This procedure generates 4,281 Δt_P^* and 3,663 Δt_S^* measurements, each corresponding station-earthquake pair where data pass selection criteria, for 89 earthquakes. A second least squares inversion determines best Δt_P^* and Δt_S^* estimates for each station from these single-earthquake Δt^* measurements, simultaneously determining the 206 station-specific Δt^* for P and S, earthquake source terms, and standard errors. The earthquake source terms are not discussed further, but are necessary to account for differences in the station subsets recording different earthquakes. Ultimately, these data will be the basis for a tomographic inversion for all of Alaska, to be presented in a subsequent study. Such an analysis is beyond the scope of the present study.

4. Results

4.1. Overview

Station values are determined from all events (Figure 3), or from one of two subsets of earthquakes at either western or eastern back-azimuths (Figure 4), along with standard errors computed from variability between measurements at a given station (Figure 5). The results indicate strong spatial correlations between nearby measurements but large variations between regions, in both Δt^* and ΔT. The per-station ΔT estimates derive from pairwise cross-correlation lags at all stations and all earthquakes in the population. The Δt^* estimates and uncertainties are determined by the procedure described above. As an alternative method of evaluating uncertainty in Δt^*, we calculate the separate reductions in variance from fitting amplitude and fitting phase spectra (from the first and second sums on the right-hand side of Equation 6), averaged over events weighted by number of observations (Figure S4). Standard deviation estimates in Δt^* are generally largest in and around basins, although the variance reduction for amplitude spectra is also largest in those locations.

Some patterns are clearer after binning stations into one of six tectonic regions (Figure 3), defined as follows. Region 1 is the Aleutian arc-backarc, bounded in the east by the edge of the Alaskan-Aleutian WBZ and by the 75 km slab depth contour to the south. Region 2 surrounds the Cook Inlet Basin, bounded by the Border Range Fault in the south and Region 1 to the north. Region 3 is the Aleutian Forearc, bounded by the limit of Alaska-Aleutian WBZ seismicity in the east and Regions 1 or 2 to the north and west. Regions 1–3 comprise normal Pacific or Yakutat plate subduction, with a clear WBZ. Region 4, the Continental Interior region, lies north of the Denali fault and east of Aleutian WBZ. Region 5 is centered on the WVF and lies south of the Denali fault but north of the Contact Fault zone, east of the Aleutian WBZ. Finally, Region 6 the Yakutat region lies south of the Contact Fault, coincident with and directly surrounding exposed deformed sediments of the Yakutat terrane. Within regions 5 and 6 the ΔT, but not the Δt^*, show a broad trend toward slower arrivals moving further east in both P and S, indicating variability at a scale large compared with array aperture (Figure 3). Figure 7 and Table S2 show mean values of Δt^* and ΔT for each region.

As a test, we computed crustal corrections to the ΔT for the crustal thickness data set of Miller et al. (2018) which provides Moho depths for 130 of the 206 stations in our study. For details, see supporting information Text S4. The crustal travel times are uncorrelated with station-mean ΔT ($R^2 < 0.02$) and correlations between ΔT_P and ΔT_S show no statistically significant change with or without accounting for crustal delays. We conclude that mantle properties, not crustal thickness, control ΔT in this region.

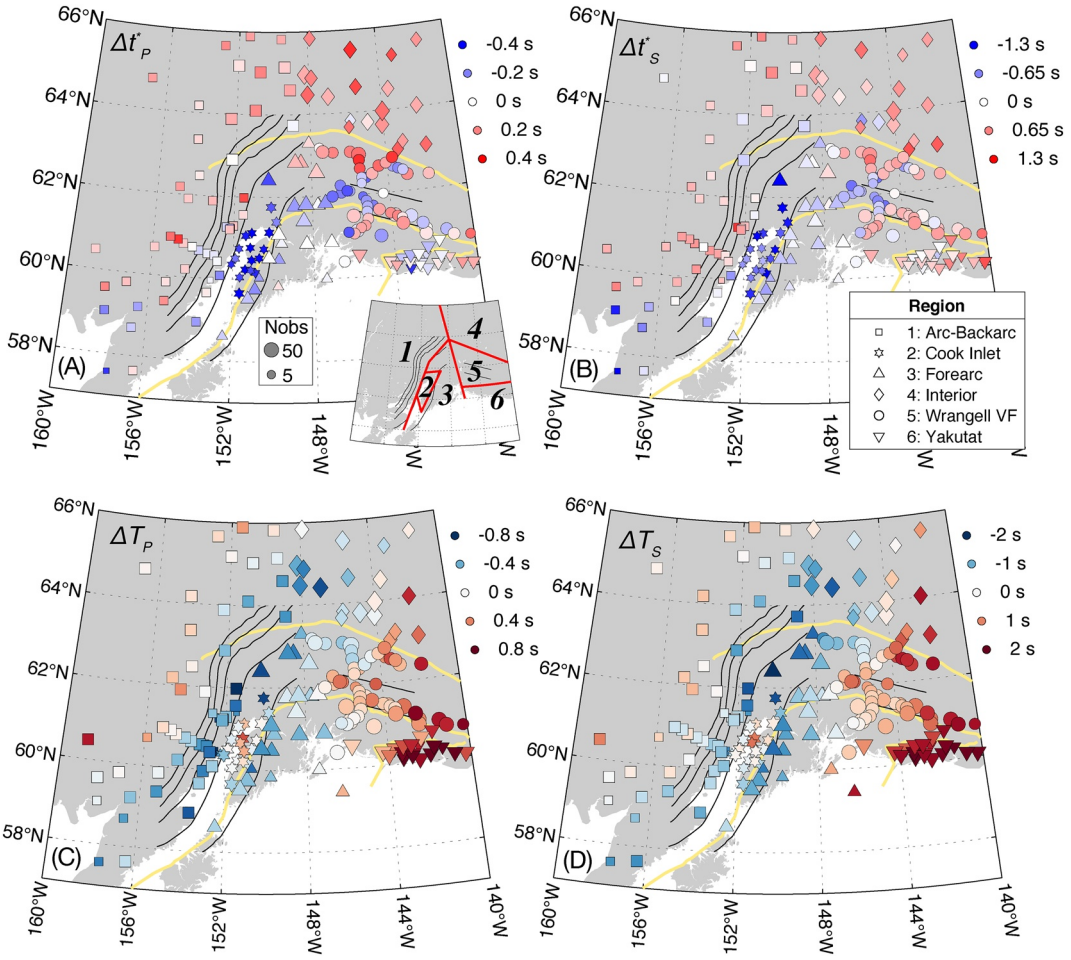

Figure 3. Station-averaged measurements, from simultaneous inversion for station terms and event terms as described in text. (a) Δt^*_P. (B) Δt^*_S.The Δt^* at each station are determined for each earthquake assumes an amplitude/phase weight ratio A of 2.0. Symbols show Δt^* values plotting at each station, with size scaled to square root of number of observations ("Nobs" in legend, left panel) and color by value, as indicated by legends to upper right. (c) Station-averaged ΔT measurements for P. (d) Same for ΔT_S. Symbol shapes indicate regions (inset) named and numbered as shown in legend on lower left. Black lines: WBZ depth contours at 40 km intervals; yellow lines: Denali, Border Ranges, and St Elias faults (Figure 1). Black lines show contours to slab surface 40 km intervals (Li et al., 2013; K. Daly, pers. comm., 2019).

4.2. Regions 1 & 3—Alaska-Aleutian Subduction

The Alaska-Aleutian subduction region has a typical geometry of subduction, showing a clear WBZ to >150 km depth and a high-velocity and high-Q subducting lithosphere (Eberhart-Phillips et al., 2006; Martin-Short et al., 2018; Nayak et al., 2020; Page et al., 1989; Ratchkovski & Hansen, 2002). The ΔT results confirm this pattern, showing some of the fastest raypaths (earliest arrivals) over the shallower part of the subducting plate and slow paths (delayed arrivals) in the backarc (Figures 3 and 6). For example, ΔT_S in the backarc (Region 1) is on average 0.49 s later than the forearc (Region 3), with that difference reaching 1.0 s for the west back-azimuthal subset (Figure 7) that is maximally sensitive to the slab structure.

The Δt^* measurements (Figures 3 and 4) show a clear difference between high attenuation in Region 1, and low attenuation in Region 3. The arc-backarc (Region 1) shows on average 0.38 s larger Δt^*_S than the forearc (Region 3). In detail, the implied gradient in attenuation arises from slab structure: there is no significant difference in Δt^*_S between these two regions for teleseisms incident from the east that barely sample the mantle wedge (Figure 4). By contrast, western back azimuth paths average 0.60 s of Δt^*_S difference between these regions, and for single stations, differences can reach 2.5 s. Raypaths from the west (chiefly from

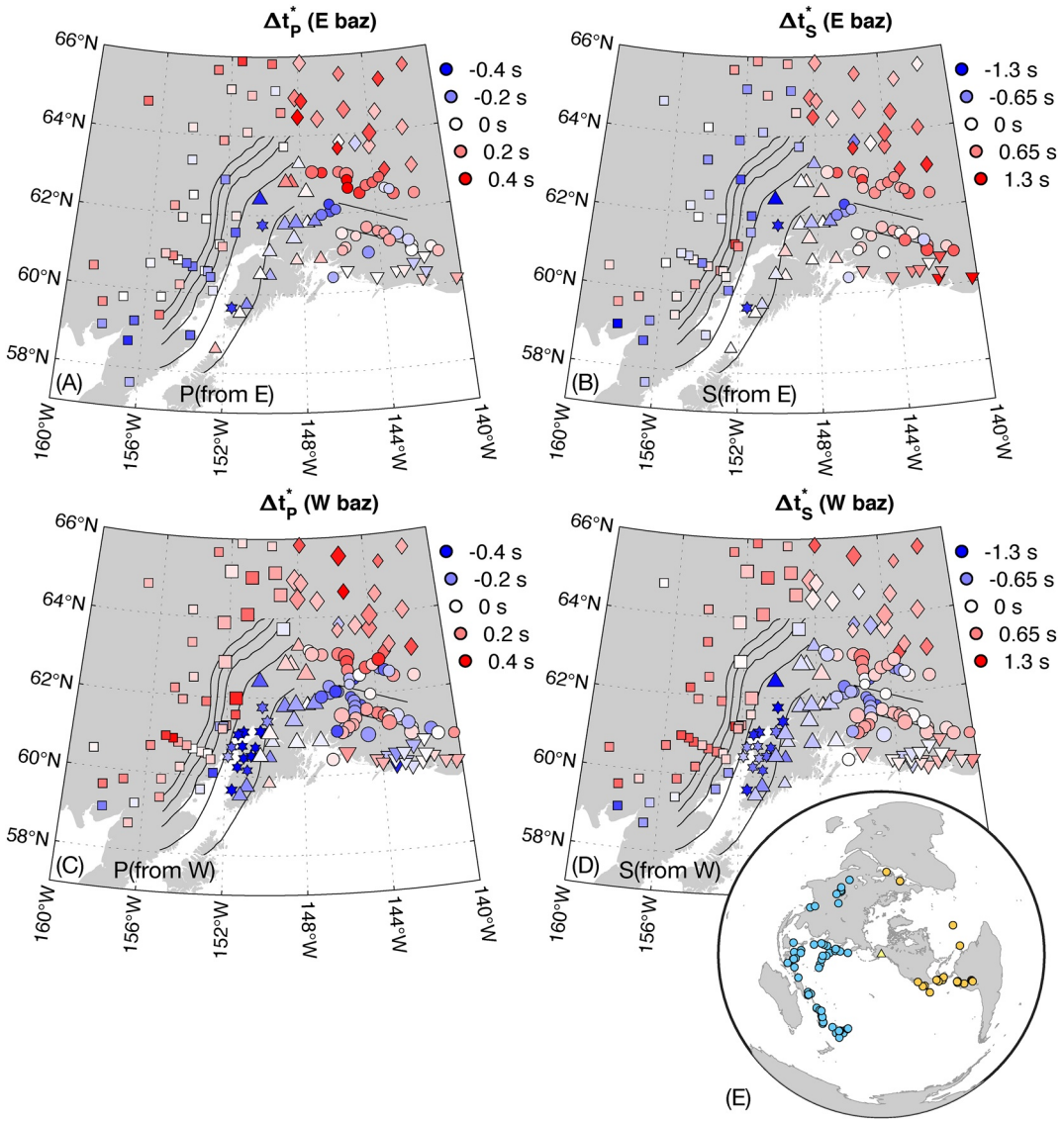

Figure 4. Differential Δt^* values per station, separated by back azimuth. (a) *P* waves, back azimuths from east. (b) *S* waves, back azimuths from east. (c) *P* waves, back azimuths from west. (d) *S* waves, back azimuths from west. (e) Global map of earthquakes colored by back-azimuthal bin. Symbols as in Figure 3.

earthquakes in western Pacific subduction zones; Figure 4e) are nearly parallel to the slab, so forearc stations record rays that spend considerable time in the cold subducting lithosphere while raypaths to back-arc stations almost entirely sample the hot mantle wedge.

These results resemble those of local attenuation studies along the Denali segment transect (Stachnik et al., 2004), and a preliminary examination of the Cook Inlet segment beneath the SALMON array (Mann & Abers, 2020). Stations located above slab depths of 80 km or greater (Region 1) not only show higher attenuation (especially for the S phase) than those in the forearc, but also show delayed arrivals and an increase in attenuation farther into the backarc. In cross section (Figure 8) there is a clear break between negative and positive Δt_S^* (and to somewhat less extent Δt_P^*) where the top of the WBZ is ~80 km deep, consistent with mantle-wedge attenuation structure of subduction zones worldwide (Abers et al., 2014, 2017, 2020). Thus, it seems likely that the teleseismic attenuation signal is dominated by the same depth range (upper 100–150 km) as dominates local earthquake attenuation. By contrast, ΔT shows negative (fast) residuals much farther downdip. Either attenuation anomalies are limited to a more restricted depth range than

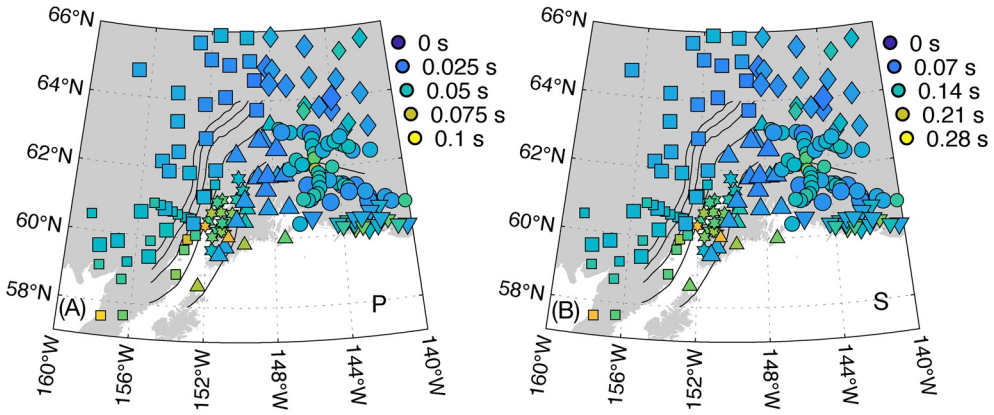

Figure 5. Standard deviation of station-specific Δt^* measurements, as formal errors in simultaneous inversion for station terms and event terms as described in text. Symbols as in Figure 3.

travel time anomalies, or teleseismic Δt^* measurements have a more limited depth sensitivity to Q than do ΔT measurements to V. A slow anomaly at +0 to +60 km along this section sits over the Cook Inlet Basin is likely a basin effect, discussed below.

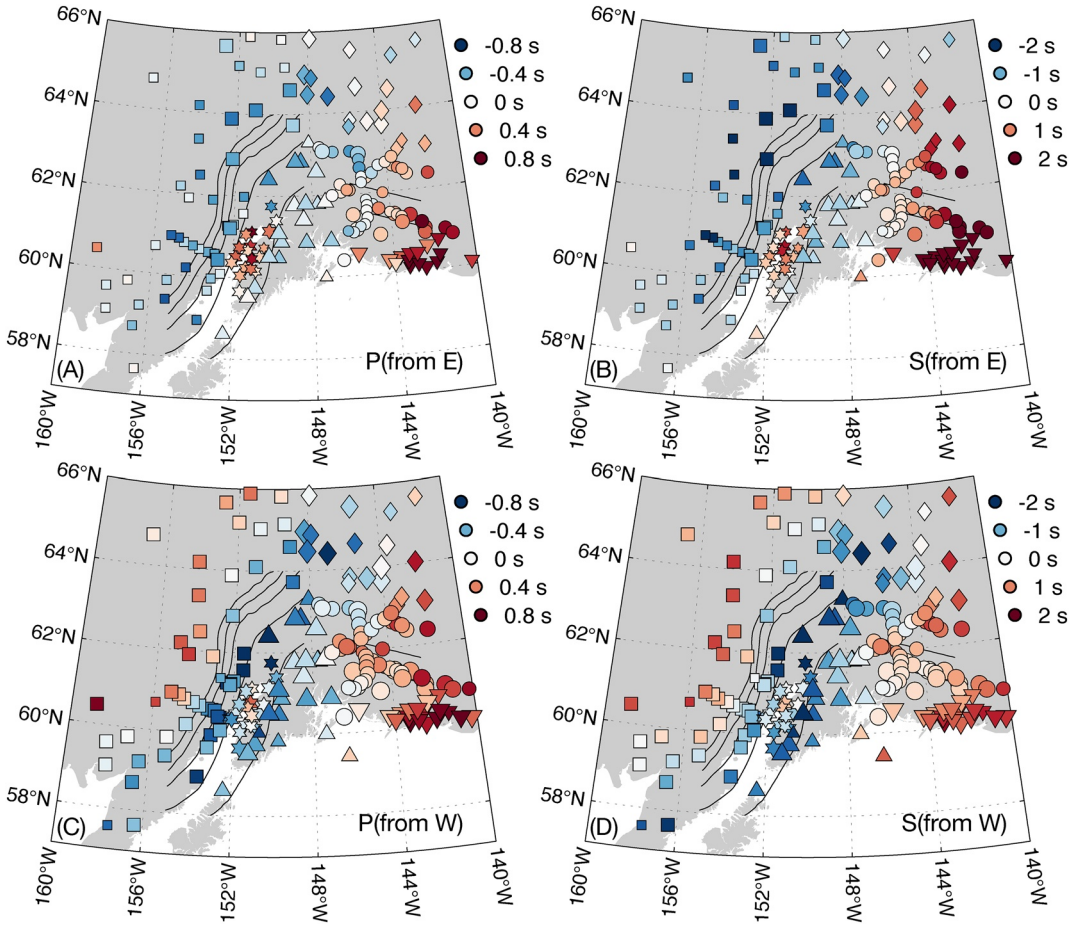

Figure 6. Differential travel-time residual (ΔT) station averages, separated by back azimuth. (a) *P* waves, back azimuths from east. (b) *S* waves, back azimuths from east. (c) *P* waves, back azimuths from west. (d) *S* waves, back azimuths from west. Symbols as in Figure 3.

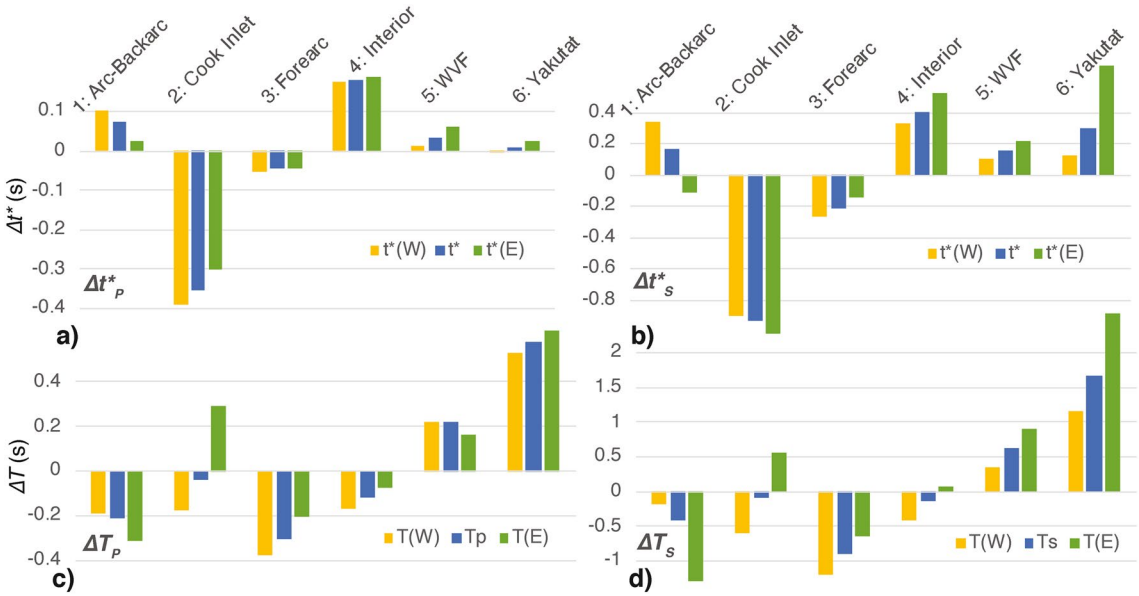

Figure 7. Station measurements averaged over regions as shown in Figure 3 and labeled (a) Δt^*_P, (b) Δt^*_S, (c) ΔT_P, (d) ΔT_S, on each, the central blue bar shows average of all measurements corresponding to Figure 3, yellow bar shows average for western back-azimuths—same data as panels c and d from Figures 4 and 6, and green bar shows for eastern back-azimuths—same data as panels A and B from Figures 4 and 6.

4.3. Region 4—The Continental Interior

The Continental Interior region shows high attenuation with the highest positive mean Δt^*_P and Δt^*_S of any region (0.18 ± 0.01 s and 0.41 ± 0.01 s respectively) but no clear spatial patterns within the region. By comparison, the ΔT measurements evince a longitudinal gradient with ΔT_S increasing from less than −1.0 s at the eastern edge of the Aleutian WBZ (~149°W) to more than +1.5 s at the Canadian border (141°W). These variations in ΔT exist in both back-azimuthal subsets (Figure 6). More positive (slow) arrivals are observed from the eastern back azimuth than from the west for all stations east of 148°W, best explained by a large, slow region somewhere east of the array at depths where rays do not cross. The long wavelength of this gradient, larger than the array, and comparison with tomography suggests a deep source relative to the width of the array, perhaps near the transition zone as seen in some tomography and inferred from discontinuity topography (e.g., Jiang et al., 2018; van Stiphout et al., 2019). Travel time but not Δt^*shows evidence of this deeper structure.

4.4. Region 5—The Wrangell Volcanic Field

The Wrangell region (Region 5) shows fast arrivals to the northwest of the WVF, and slower arrivals elsewhere, dominated by slow arrivals with mean ΔT_S and ΔT_P of 0.64 ± 0.03 s and 0.22 ± 0.01 s respectively. In both *S* and *P*, arrivals become slower toward the south where thick Yakutat sediments occur (see below). The pattern in ΔT differs from that of the Alaska-Aleutian subduction system which shows fast paths associated with subducted lithosphere. Some of the pattern in ΔT is dominated by the strong increase in travel-time delays toward the eastern edge of the data set, as discussed above for Region 4, making all ΔT east of 144°W anomalously positive (Figures 3c and 3d).

By comparison, the Δt^* pattern across the WVF more resemble those within the Cook Inlet—Kenai region of Alaska-Aleutian subduction. There is a sharp boundary between low-attenuation regions just south of the WVF (the forearc) transitioning to high-attenuation regions further north (the hot mantle wedge) over distances as short as ~30 km (Figure 9). This step is at least 1.0 s in Δt^*_S and 0.6 s in Δt^*_P. In other words, attenuation here matches expectation for a subduction zone while travel times do not so clearly. Further south, Δt^* changes gradually back to higher attenuation south of the Border Ranges Fault or east of 145°W,

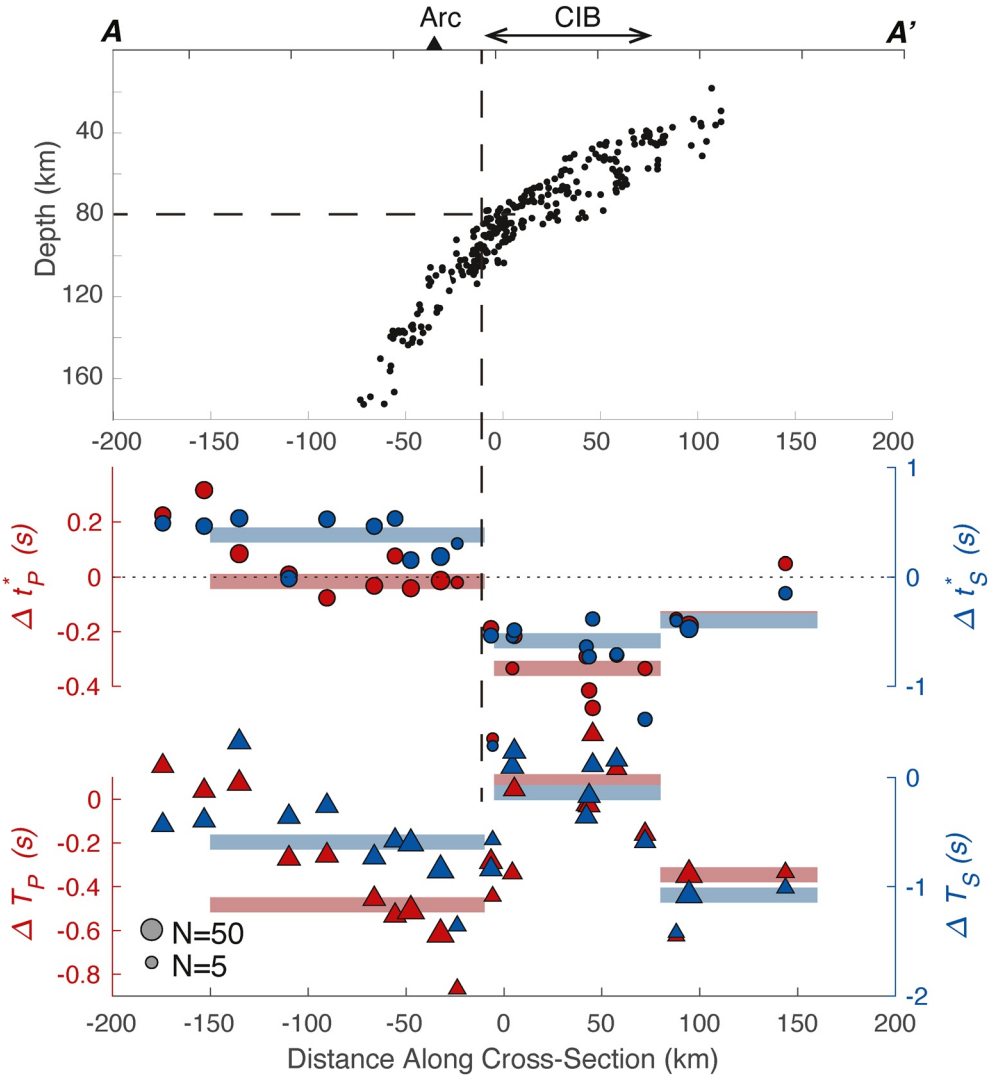

Figure 8. Cross section of results and seismicity through Cook Inlet; A-A' from Figure 1. Top: local seismicity from AEC catalog, 2016–2018 for earthquakes within 25 km of cross section, with depth errors <1 km. Triangles: volcanic arc. CIB: Cook Inlet Basin. Middle: station averages of Δt^* for P (red, left axis) and S (blue, right axis), for all stations within 50 km of the cross section on Figure 1. Bottom: same for ΔT. Dashed line shows transition from high to low attenuation. Horizontal bars show median values for segments; red: P, blue: S. Symbol size scaled by number of observations, key in lower left. Note ΔT for this region is all negative; values are relative to the entire study area.

a pattern persisting into Region 6. This behavior is not seen in Regions 1–3 and indicates additional factors influencing Δt^*.

In cross section (Figure 9) the northern low-attenuation region lies above where the slab is ~40–110 km deep, with Δt^* substantially increasing farther north. The region of high Δt^* located south of the Border Ranges fault does not have an analog in the Alaska-Aleutian subduction region, and may relate to unusual structure of the Yakutat collision south of that fault zone. Overall the attenuation measurements have a clearer relationship to shallow subduction geometry here than travel times, which are generally slow throughout.

4.5. Regions 2 & 6—The Cook Inlet Basin and the Yakutat Terrane Sediments

Region 6 is dominated by the Yakutat basin, a marine sedimentary section ~10 km thick (Trop & Ridgway, 2007) associated with very low crustal velocities (Berg et al., 2020). Slow arrivals in this region are

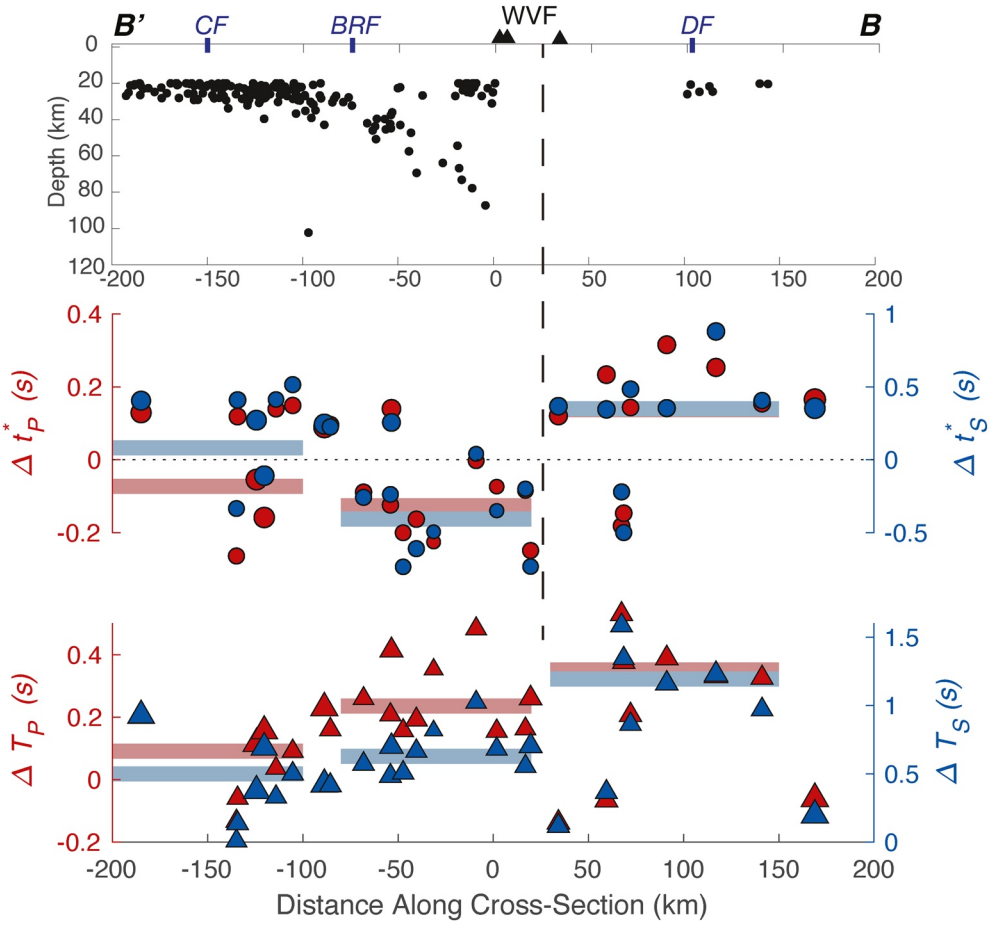

Figure 9. Cross section through Wrangell Volcanic Field (WVF), B-B' on Figure 1. Top: local seismicity from AEC catalog, 1999–2018 for earthquakes within 25 km of cross section, with depth errors < 1 km. Triangles: volcanic arc. Middle: station averages of Δt^* for P (red, left axis) and S (blue, right axis), for all stations within 50 km of the cross section on Figure 1. Bottom: same for ΔT. Vertical dashed line shows transition from high to low attenuation. Symbol size and horizontal bars as in Figure 8. Terrane bounding faults: CF, Contact Fault; BRF, Border Ranges Fault System; DF, Denali Fault.

partly due to the thick sedimentary section; on average this is the slowest region within the study area with ΔT_S & ΔT_P of 1.67 ± 0.03 s and 0.58 ± 0.02 s respectively, and shows little dependence on back azimuth. The Cook Inlet Basin, Region 2, contains a sedimentary cover sequence reaching depths approximately 8 km at its deepest parts (Plafker & Berg, 1994; Shellenbaum et al., 2010; Smith & Tape, 2020), and substantially delayed arrivals relative to surrounding regions, by 0.81 and 0.27 s for ΔT_S and ΔT_P, respectively.

By contrast, the Δt^*measurements show little clear correlation with the presence of thick sediment sequences. In the Yakutat region (Region 6) Δt^*_P shows variable values that average near zero, while Δt^*_S is moderately positive (0.29 ± 0.02 s) (Figures 3 and 6). Within the Cook Inlet Basin (Region 2) mean Δt^*reaches the most negative values of any region (−0.35 ± 0.01 and −0.94 ± 0.04 for P and S respectively). We note that this basin also lies above a cold subducting plate.

4.6. Variation With Frequency Dependence

We calculate Δt^* assuming frequency independence ($\alpha = 0$) in most of the results presented here, but also test a weak frequency dependence of $\alpha = 0.27$ for comparison to previous attenuation studies (e.g., Abers et al., 2014). The frequency-dependent attenuation operators Δt^*_{0ij} are effectively the attenuation at 1 Hz, under the assumption that the frequency dependence holds between the frequencies of measurement

(0.05–0.5 Hz) and 1 Hz. The two estimates (for $\alpha = 0$ and $\alpha = 0.27$) are highly correlated with correlation coefficients R of 0.997 and 0.995 for P and S respectively (Figure S5). For P waves the two sets are equal within uncertainty, while Δt_S^* for $\alpha = 0.27$ are 86 ± 1% of those for $\alpha = 0$. The slight decrease in apparent attenuation is consistent with attenuation at the highest frequencies controlling the Δt^* estimates (Stachnik et al., 2004), which in this case is 0.5 Hz, as $(0.5/1.0)^{0.27} = 83\%$, approximately what is observed.

5. Discussion

5.1. Sources of Attenuation or Velocity Anomalies

In the Alaskan-Aleutian subduction region, relatively slower arrivals (more positive ΔT) occur northwest of the arc (Region 1) compared to the forearc (Region 3), consistent with subduction of a cold, fast plate beneath a warm backarc asthenosphere. This feature has been seen in local (e.g., Kissling & Lahr, 1991; Nayak et al., 2020; Zhao et al., 1995) and teleseismic tomography (e.g., Frost et al., 2020; Gou et al., 2019; Jiang et al., 2018; Martin-Short et al, 2018). In comparison, Δt^* shows that a transition from low forearc attenuation to high sub-arc attenuation is almost directly beneath the volcanoes, near the 75 km slab contour (Figure 8). This is ~120 km southeast of the sub-arc/fore-arc transition depicted by the differential travel times, and hints at a difference in the sampling of the Earth by these respective data types. The Δt^* pattern closely matches that seen in local-earthquake attenuation studies beneath Cook Inlet and the Denali region (Mann & Abers, 2020; Stachnik et al., 2004), supporting the suggestion that the mantle wedge above the downgoing plate controls teleseismic body wave attenuation. Seismicity is insufficient beneath the WVF for local-earthquake attenuation estimates, so we rely upon the teleseismic measurements and the comparison with nearby regions to infer attenuation beneath the WVF.

One explanation for the difference between travel-time and attenuation patterns is that they are sensitive to underlying mechanisms with different characteristic depths. The Δt^* results are best explained if attenuation is most sensitive to high temperature near the solidus, which is likely achieved at a relatively confined depth range near 50 km where much melt equilibrates in arcs (e.g., Lee et al., 2009). By contrast, the elastic or anharmonic contribution of temperature to V_S remains roughly constant at all temperatures, so would be strongly affected by the contrast between cold slabs and hot surrounding mantle at all depths. Recent experiments indicate a strong sensitivity of attenuation exists to temperature at near-solidus conditions (Takei, 2017; Yamauchi & Takei, 2016) or to small degrees of melt just above the solidus (Faul et al., 2004). Depth-dependent attenuation estimates in Tonga (Wei & Wiens, 2018) support a shallow-mantle origin for the strongest attenuation anomalies near arcs. To emphasize this point, Figure 10 shows estimates of the accumulated velocity difference (i.e., ΔT) and attenuation difference (Δt^*) between a cold slab-like geotherm and adiabatic mantle wedge, assuming the calibration of Yamauchi and Takei (2016; Takei, 2017). This calculation, detailed in supporting information Text S3, shows that Δt^* is controlled almost entirely by temperature in the upper 150–200 km while ΔT depends on thermal contrasts throughout the upper mantle. Note that this analysis does not account for any additional anelastic effects owing to *in situ* melt (Faul et al., 2004), which is also thought to be confined to the upper 200 km of mantle (e.g., Hirschmann, 2006). Thus, the differences measured in this study between integrated attenuation and velocity anomalies are likely a consequence of the different depth distributions of elastic and anelastic effects.

Similar to the Alaska-Aleutian arc, patterns of low attenuation in the WVF provide evidence for subduction. The ΔT anomalies (Figures 3c and 3d) show fast arrivals in P and S persisting hundreds of km north of the WVF, particularly for west back-azimuths (Figures 6c and 6d) consistent with a deep aseismic extension of the slab here similar to that imaged west of Cook Inlet. By contrast, a northward transition from low attenuation (negative Δt^*) to high occurs almost directly beneath the WVF volcanoes (Figure 9). This pattern resembles that seen in Cook Inlet (Figure 8), although the extrapolation of the surface gradient downwards intersects the Wrangell slab surface at slightly greater depths. This pattern is consistent with a hot mantle wedge north of the cold subducting Yakutat lithosphere beneath the WVF. Again, the differences are consistent with attenuation being more sensitive to shallow mantle features while travel times integrate deeper structure.

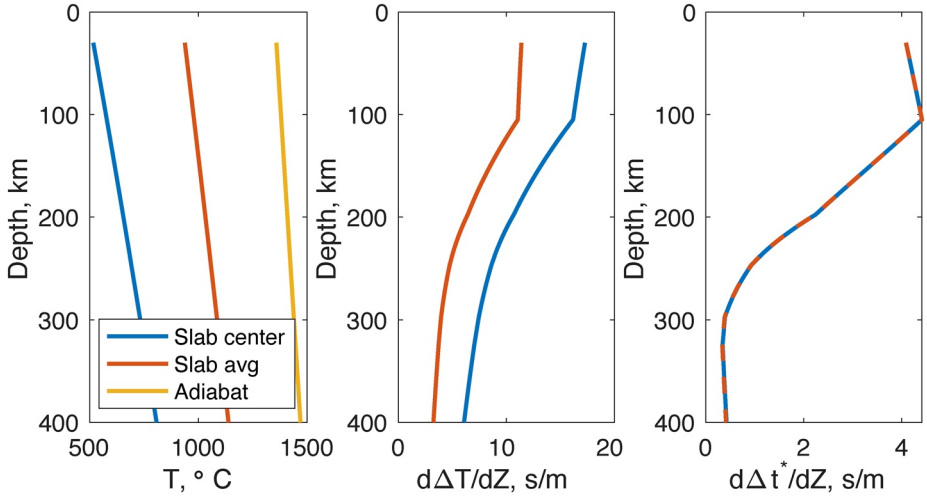

Figure 10. Model of slab temperature differences between interior and ambient mantle, and resulting velocity or attenuation, described in Supporting information Text S3. (a) Temperatures in slab center, surrounding adiabatic mantle, and average of the two, varying with depth. (b) Resulting velocity differences within slab relative to ambient adiabatic mantle, expressed as travel-time sensitivity $d\Delta T/dz$. For these parameters, the integrated anomaly is 2.49 s for the slab average or 4.05 s for the slab center. (C) Resulting attenuation differences within slab relative to ambient mantle, expressed as $d\Delta t^*/dz$. For these parameters, the integrated anomaly is $\Delta t^* = 0.78$ s for both the slab center and midpoint temperature.

5.2. Evidence for Wrangell Subduction in the Continental Interior

In the Continental Interior region (Region 4), east and north of the Aleutian WBZ intermediate-depth seismicity, some velocity imaging studies show a high-velocity subducting slab extending east of the edge of the WBZ seismicity (Jiang et al., 2018; Wang & Tape, 2014), while others do not (Berg et al., 2020; Martin-Short et al, 2018). On average, the continental interior shows the highest Δt^* (most attenuation) of any region (Figure 6). This broad swath of high attenuation extends the Arc/Backarc region (Region 1) east along strike, suggesting a similar origin. The high attenuation northwest of Cook Inlet appears to stem from mantle wedge processes related to sub-arc melt production, suggesting that high attenuation east of 147°E may likewise result from Yakutat slab subduction beneath the WVF.

The Continental Interior region in fact shows slightly higher Δt^* than the adjacent Backarc for both P and S, and this pattern extends to the north edge of our data set hundreds of km from the volcanic arc (Figure 3). This somewhat counter-intuitive observation indicates that arc-back-arc thermal structure alone cannot explain attenuation patterns. Other processes, perhaps associated with the leading edge of North American lithosphere, are likely to contribute. For example, the region east of 150°W corresponds to a north-south zone of diffuse deformation accommodating differential motion of western Alaska from North America (Finzel et al., 2011). Diffuse deformation could increase attenuation through some combination of dissipative heating, strain-induced grainsize reduction, and secondary flow. A similar correlation between Δt^* and tectonic deformation has been observed in Iberia (Bezada, 2017). However, it is difficult to rule out other explanations without tomographic imaging over a larger area and extensive physics-based modeling.

In the Cook Inlet region (Figure 8) and the Denali segment (Stachnik et al., 2004), low attenuation occurs at stations overlying slab depths of < 80km. The pattern seen here from teleseismic signals matches the one prior attenuation study in Alaska using local-earthquake signals (Stachnik et al., 2004). The WVF region (Figure 9) shows similarly low attenuation north of where the slab descends to mantle depths (>40 km), and then manifests a transition to higher attenuation at a slab depth of ~100 km. Intermediate-depth seismicity in both regions confirms the presence of the slab (Page et al., 1989; Ratchkovski & Hansen, 2002). Thus, seismic attenuation in the WVF corridor shows clear evidence of a cold shallow forearc abutting a deeper hot wedge, characteristics of subduction zones worldwide (Abers et al., 2017, 2020).

Still, the Yakutat-Wrangell segment shows complexity not seen in the "normal" subduction segment farther west. There is a zone of high attenuation directly south of the WVF between the Border Ranges Fault and Contact Fault (Figure 9) with pockets of high attenuation throughout. A relatively high-attenuation region near 61°N, 145°W, just south of the WVF, extends eastward in Δt_S^* but not Δt_P^* (Figure 3). Travel times here exhibit a large westward trend to very positive ΔT in easternmost Alaska discussed above (Figures 3c and 3d). This is the one region where the attenuation signal does not have a clear relationship with upper-mantle thermal structure, and may indicate complex crustal processes related to the Yakutat collision here, or the influence of a deeper hot region that creates the very delayed ΔT being near enough to the solidus to affect attenuation.

Overall, the teleseismic Δt^* results strongly resemble local earthquake attenuation (Stachnik et al., 2004) but provide much wider areal coverage. This study also benefits from the WVLF and SALMON seismic array data that boosts resolution in two critical regions, showing that the pattern in teleseismic attenuation generally resembles that seen from local earthquake data in subduction zones worldwide.

5.3. Sedimentary Structures—Attenuation and Travel Times

The Cook Inlet Basin (Region 2) shows more positive (late) ΔT compared with surrounding regions, consistent with the thick sequence of low-velocity sediments. However, Δt^* is negative in the same place and reaches some of its most negative values throughout the study area, indicating very little attenuation. A similar, although less striking, pattern is seen in the shallower Copper River Basin (Figure 1), where positive (slow) ΔT is accompanied by negative (less attenuating) Δt^*. The thick pile of Tertiary sediments in the Yakutat area (Region 6) shows very slow travel times, and moderate attenuation, in a pattern that has some similarities although overall slower and more attenuating.

The influence of sediments from the Cook Inlet Basin and Yakutat Terrane (Plafker & Berg, 1994; Smith & Tape, 2020) on travel times can be easily explained. In the Cook Inlet Basin, a 5 km sequence with mean S-wave velocity (V_S) of 2.2 km/s surrounded by basement of 3.5 km/s, as estimated in recent high-resolution velocity models (Figure S8 of Nayak et al., 2020), would explain the observed 1.0 s difference in ΔT_S between regions 3 and 2. The P-wave velocity (V_P) has been observed to vary from about 5.0 in the basin to 6.5 km outside, averaged over the upper 10 km (Nayak et al., 2020). That difference explains the 0.35–0.40 s difference in ΔT_P observed between the two regions.

Very low attenuation (negative Δt^*) observed in the basins is harder to understand. The increased attenuation typically associated with porous sediments at high frequencies (e.g., Müller et al., 2010), does not seem to be a factor here for 0.05–0.5 Hz teleseismic body waves. Wavelengths for S waves exceed basin thickness in our attenuation measurement band, so direct basin effects may be minor at finite frequencies. The Cook Inlet Basin sits in the cold part of the forearc typically associated with very low temperatures and little attenuation (Abers et al., 2014, 2017). It is possible that the low attenuation seen here is just an effect of the underlying plate. However, the attenuation is not just low in the basins but also slightly lower than on either side (e.g., Figures 3 and 4), suggesting additional factors. In China and Iberia-Morocco, very low attenuation has been attributed to cold and rigid lithosphere underlying basins, a potential factor for basins that form atop undeforming continental blocks (Bezada, 2017; Deng et al., 2021). However, in our case the apparent attenuation is markedly less (more negative Δt^*) than adjacent parts of the cold subducting plate to the southeast, with no lithospheric boundary in between, and the sharpness of the horizontal gradient in observed Δt^* over <20 km (Figure 8) makes it unlikely that deep-seated lithospheric structure can be responsible for this phenomenon.

Perhaps, basin amplification effects are altering the spectra in ways not accounted for by the attenuation model (Equations 2–5). Frequency-dependent amplification has been well documented in the Cook Inlet Basin and to lesser extents in other Alaska basins (Moschetti et al., 2020), showing 6–14 db S-wave amplification in the 0.1–0.5 Hz frequency band (Smith & Tape, 2020). To test the effects of possible amplification, we re-ran the spectral fits varying the weighting factor A between fits to amplitude and phase (Equation 6). Basin resonance effects could be altering amplitudes in a manner that steepens the spectral slope and hence mimics negative differential attenuation, but it seems unlikely that they would be altering the phase spectra

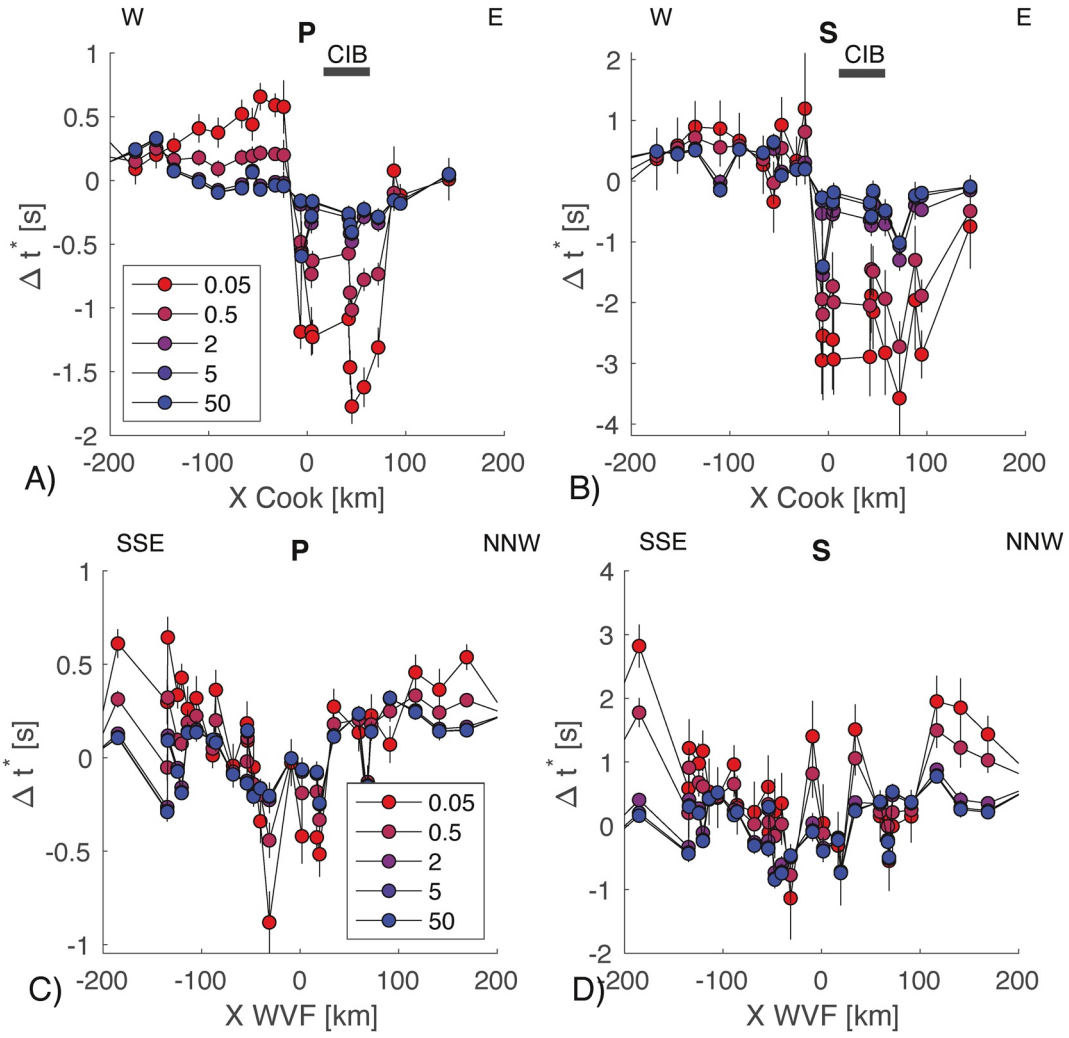

Figure 11. Attenuation operators along dense transects, varying the weight, A, of fitting amplitude spectra relative to phase spectra. Smaller A, indicated by legend, corresponds to increased fitting of phase terms. (a) *P*-wave results along the Cook Inlet transect (Figure 8). (b) *S*-wave results along the Cook Inlet transect. (c) *P*-wave results along the Wrangell Volcanic Field transect (Figure 9). (d) *S*-wave results along the Wrangell Volcanic Field transect. CIB: Cook Inlet Basin. Stations shown all lie within 50 km of the cross section lines shown on Figure 1; locations are same as Figures 8 and 9.

in the same way. However, we find that increasing the weight on fitting phase spectra ($A < 1.0$) actually exaggerates the negative Δt^* anomaly associated with the Cook Inlet Basin, indicating that the phase spectra are consistent in sign (i.e., spectral slope direction) with amplitude spectra, although scatter increases (Figure 11). This pattern indicates that higher frequencies are delayed relative to the low-frequency arrival beyond the physical dispersion associated with the amplitude decay, giving the appearance of additional attenuation in phase compared to that inferred from amplitude decay. This is not obviously consistent with short-period basin amplification. Possibly, short-scale wavefront healing at low frequencies could effectively speed up longer periods; additional modeling would be necessary to test this possibility.

Finally, we note that the Cook Inlet Basin shows substantial back-azimuthal variation, perhaps indicative of strong azimuthal anisotropy which might substantially affect attenuation measurements in unexpected ways. ΔT for both P and S is markedly slow in this region for eastern arrivals, and much less so for western arrivals. The sharp gradients in ΔT at the edge of the basin confirm that this signal has a shallow origin. Unfortunately, a lack of usable attenuation measurements from eastern back azimuths precludes a clear picture of how this anisotropy might affect Δt^* values. If anisotropic Q and velocity are correlated here,

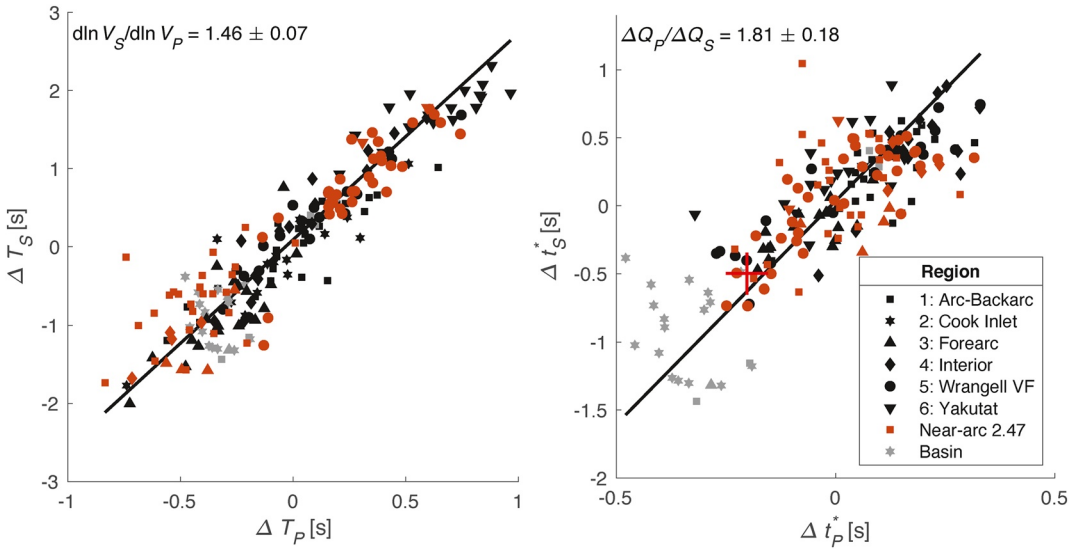

Figure 12. (Left) Station-averaged *P* versus *S* differential travel times. (Right) Station-averaged *P* versus *S* differential attenuation. Symbols indicate region as shown in legend. Gray symbols: stations in Cook Inlet or Bristol Bay basins; red symbols: stations within 100 km of the arc volcanoes or 100 km WBZ isobath. Thick black line shows orthogonal regression through full data set; inferred slope (divided by *Vp*/*Vs*) shown in upper left, with 95% uncertainties from bootstrap. Red plus sign shows Δt^*_{ref} for *P* and *S*, as described in text.

however, the inhomogeneity in back azimuths for attenuation measurements may exaggerate the amplitude of the low attenuation values measured in this basin.

These findings confirm that sedimentary basins complicate use of teleseismic attenuation measurements. Still, the attenuation signal preserves the essential nature of the underlying mantle thermal structure, unlike the travel times.

5.4. Estimates of Q^{-1}

To compare with laboratory and other seismic measurements, we convert the station-averaged Δt^* to path-averaged $\bar{Q}^{-1}$ beneath each station, from the integrated absorption $t^* = L / \bar{Q}V$. We assume the relevant path length L over which Q varies is the raypath between the base of the crust (30 km depth) and the base of the low-velocity zone (220 km depth), with constant $V_P = 8.05$ km/s and $V_S = 4.45$ km/s from PREM (Dziewonski & Anderson, 1981), and typical a teleseismic incidence angle (29°). To convert differential Δt^* to the total t^* accumulated in the upper mantle beneath each station, t^*_{um}, we assume $t^*_{um} = \Delta t^* + \Delta t^*_{ref}$ where Δt^*_{ref} corresponds to the value that would be estimated for paths with no attenuation in the relevant depth range (Eilon & Abers, 2017). To account for measurement error, Δt^*_{ref} is chosen as the observed value that lies lower than 95% of all station-averaged Δt^* for either *P* or *S* (Figure 12), under the assumption that cold slab paths have negligible attenuation in the upper 220 km. This analysis uses only stations that lie outside of the Cook Inlet Basin (Region 2) and the Bristol Bay Basin (stations west of 157°W), to avoid the basin effects discussed above. Calculated in that fashion, we find Δt^*_{ref} of −0.202 and −0.498 s for P and S, respectively (indicated by the red cross on Figure 12).

The full non-basin data set gives mean 1000 / $\bar{Q}$ as 8.8 ± 0.1 or 13.0 ± 0.1 for *P* and *S* respectively (2-σ uncertainties in means), corresponding to median quality factors of $\bar{Q}_P = 109$ and $\bar{Q}_S = 70$. These estimates vary regionally (Table 1); for example, 1000 / $\bar{Q}_S$ varies from 6.8 ± 0.3 to 14.0 ± 0.3 ($\bar{Q}_S$ varies between 147 and 71) between the forearc (Region 3) and backarc (Region 1). Much stronger attenuation (1000 / $\bar{Q}_S \sim$ 40) is inferred from a similar calculation beneath the Juan de Fuca ridge where substantial melt is present (Eilon & Abers, 2017). These absolute values are similar to global and regional surface-wave studies of the uppermost mantle, which show global average 1000 / $\bar{Q}_S \sim$ 12–15 at 100–200 km depth, varying from 8 to 16 with tectonic region (e.g., Dalton et al., 2009). Surface waves sample roughly 10× longer periods than the

Table 1
Regional Regressions on ΔT and Δt^*

Region	Name	dQ_P/dQ_S [a]	$d\ln V_S/d\ln V_P$ [a]	$1000 / \bar{Q}_P$ [b]	$1000 / \bar{Q}_S$ [b]
–	All	1.81 ± 0.19	1.46 ± 0.06	–	–
–	No Basin	1.85 ± 0.19	1.46 ± 0.07	8.82 ± 0.07	13.02 ± 0.1
1	Arc/backarc	2.87 ± 1.15	1.21 ± 0.18	9.43 ± 0.19	14.00 ± 0.31
2	Cook Inlet	–	1.36 ± 0.30	–	–
3	Forearc	2.05 ± 0.74	2.14 ± 0.66	6.02 ± 0.32	6.81 ± 0.30
4	Cont. Int.	2.82 ± 1.55	1.58 ± 0.15	14.22 ± 0.34	18.37 ± 0.72
5	Wrangell	1.47 ± 0.18	1.61 ± 0.27	8.04 ± 0.24	11.93 ± 0.32
6	Yakutat	2.09 ± 1.16	0.89 ± 0.22	7.33 ± 0.44	15.47 ± 0.63
7	Near-arc	2.47 ± 0.78	1.44 ± 0.12	8.10 ± 0.14	12.10 ± 0.22

[a]Estimates assume $V_P/V_S = 1.81$, from orthogonal regression. Uncertainties are 2-σ from bootstrap. Results excluded where uncertainty exceeds 2.0. Region 2 was removed from Q estimates. [b]$1000 / \bar{Q}$ are path averages over upper 220 km as described in text, with 2-σ uncertainties in mean.

teleseismic body waves here, indicating a fairly minimal frequency dependence between ~100 and ~10 s period. However, different regions are averaged in this comparison so some frequency dependence may be balanced by regional variation. Also, the choice of Δt^*_{ref} is somewhat ad hoc; choosing the lowest observed Δt^* rather than the 5th percentile will reduce $\Delta t^*_{S,ref}$ by 0.24 s and increase the mean $1000 / \bar{Q}_S$ by 4.9.

High-frequency local body wave estimates (assuming frequency independence) show $1000 / \bar{Q}_S$ of 3–4.5 for paths in the Denali segment (Stachnik et al., 2004). These paths have geometries that are analogous to those here, but are shorter and indicate 3–5 times lower $1000 / \bar{Q}_S$. These high-frequency data also show 5–8× higher attenuation in the wedge than adjacent slab, a greater contrast than the factor of 2–3× variation in $1000 / \bar{Q}_S$ seen in the present study between the Forearc region and either the Arc or Interior. This discrepancy reflects the fact that shorter paths in the local study allow better separation of rays sampling the slab versus the wedge than is possible with teleseisms.

Those measurements are most sensitive to frequencies near 10 Hz, which are 30 ± 10 times higher than the maximum frequencies sampled here. The difference in attenuation could be explained by a frequency dependence of f^α where $\alpha = 0.3$–0.5 (since $30^{0.3–0.5} = 2.8$–5.5). That α is slightly larger than determined experimentally (Jackson & Faul, 2010; Takei, 2017) but the paths are not identical. Alternatively, the Cook Inlet and Wrangell regions may have quantitatively higher attenuation than the Denali segment, a consequence of more abundant melt as reflected by extensive volcanism. Other volcanically productive arcs show high-frequency attenuation more similar to the teleseismic estimates here. For example, in the Mariana back-arc means Pozgay et al. (2009) estimated a maximum $1000/Q_S$ of 30, and Rychert et al. (2008) estimated $1000/Q_S$ of 23 and 15 beneath Nicaragua and Costa Rica respectively. Overall, the most attenuating regions here are quantitatively consistent with a wide variety of other subduction zone studies. Future work would be needed to more carefully account for regional variability and the role of frequency dependence.

5.5. Covariance Between *P* and *S* Measurements

The covariation of ΔT for P and S provides a measurement of $d(\ln V_S)/d(\ln V_P)$, the covariation of S with P velocities. That can offer insight into the processes that cause elastic moduli to vary. At one extreme the bulk and shear moduli can vary similarly such that $d(\ln V_S)/d(\ln V_P)$ ~1–1.5, as expected for anharmonic temperature variations or some melt fabrics, while near-solidus temperature variations or high-aspect-ratio fluid distribution lead to stronger shear modulus reduction than bulk modulus, with $d(\ln V_S)/d(\ln V_P) \geq 2$ (e.g., Karato, 1993; Takei, 2002). Similarly, covariation between Δt^*_P and Δt^*_S provides a measurement of the relative variation of the P and S attenuation dQ_P / dQ_s (see Supplemental Information). For attenuation in

shear modulus only, $dQ_P \,/\, dQ_s$ should be $4 \,/\, 3\left(V_S \,/\, V_P\right)^2$, or 2.25–2.43 for $V_P/V_S = 1.73$–1.81, whereas lower values of this ratio indicate bulk attenuation is significant.

For the entire data set, we find $d(\ln V_S)/d(\ln V_P) = 1.46 \pm 0.07$ (95% uncertainties from bootstrap), consistent with thermal or equilibrated melt processes, and $dQ_P \,/\, dQ_s = 1.85 \pm 0.19$ (1.81 ± 0.18 when basins are included; Table 1) indicating some relaxation of bulk moduli (Figure 12). These correlations lie within the range of similar observations at other subduction zones, some of which also indicate the possibility of bulk attenuation. For example, Wei and Wiens (2020) document a region of resolvable bulk-modulus attenuation in the mantle centered beneath the Lau back-arc spreading center, attributed to abundant melt forming there rather than beneath the arc. The different raypaths contributing to the Alaska array average sample subducting lithosphere, back-arc mantle, and subcontinental mantle so it is difficult to be sure exactly where the bulk attenuation occurs. For just the stations near the volcanic arcs (within 100 km of a volcano or the 100-km WBZ contour on Figure 1), we find $dQ_P \,/\, dQ_s = 2.47 \pm 0.78$ (labeled Near-arc in Table 1). This measurement allows the possibility that all variation lies in shear-modulus attenuation in the subduction mantle wedge directly beneath the arc, although uncertainties are large. The range of values in ΔT or Δt_P^* are too limited within any other single subregion to obtain regression with smaller uncertainties, although some variations exist (Soto Castaneda, 2020; Supporting information). In particular, high $dQ_P \,/\, dQ_s$ is associated with the backarc Regions 1 and 4, indicating that the high attenuation there is a shear-modulus-controlled process. Bulk attenuation is only indicated for Region 5 coincident with the WVF, $dQ_P \,/\, dQ_s = 1.47 \pm 0.18$, where extensive melt transport may be occurring (see Supplemental Information Text S2). In summary, there is evidence for some regions in which bulk-modulus attenuation is likely although their relationship to volcanic arc source regions seems to depend upon the arc segment, indicating that the quantity and perhaps type of melt may be relevant.

5.6. Covariance Between ΔT_S and Δt_S^* Measurements

Although travel-time and attenuation measurements vary in complex ways, as discussed above, a weak correlation exists between the two for S waves (Figure 13, left). With basin sites eliminated, the correlation coefficient between the two measurements is 0.295, statistically significant but showing considerable scatter. We focus on non-basin data Regions 1 and 3 where data are controlled by Aleutian subduction in a relatively simple manner (Figure 13, right), and find positive correlation between ΔT_S and Δt_S^* ($R = 0.514$; $p = 2.9 \times 10^{-6}$, slope = 0.446 s/s), as expected for predominantly thermal control. In detail there is still considerable scatter, likely due to the differing depth sensitivity discussed above. The estimate of absolute $\bar{Q}^{-1}$ discussed in Section 5.4 allows these trends to be compared with laboratory-based models for attenuation. Comparison with five different predictions demonstrates variability in the laboratory-based models, but all generally show the same correlation as observed here. Some of the similarity is expected, in that physical dispersion produces a common connection between attenuation and velocity reduction, but still these comparisons confirm that in simple settings the teleseismic attenuation and velocity data are linked by a common process. The lack of correlation elsewhere is a consequence of the complications discussed above.

6. Conclusions

Teleseismic body-wave attenuation varies substantially across the Alaska subduction zones. Our results agree with previous local earthquake attenuation measurements where they overlap spatially, and complement teleseismic velocity studies. Specifically, the Δt^* measurements show a boundary between the hot mantle wedge and the cold forearc in both the Alaska-Aleutian system and the Yakutat subduction system. The former matches well the observations from local-earthquake attenuation studies in the Cook Inlet and Denali regions of a boundary near where the subducting plate interface reaches 75 km depth. The presence of a similar feature beneath the Wrangell Volcanic Field provides evidence for typical subduction thermal structure. These measurements contrast with ΔT, which shows high-velocity slabs extending to depths past WBZ seismicity but relatively little evidence for the shallow hot mantle wedge. That difference is likely due to the importance of near-solidus temperatures in reaching high $1/Q$, a condition that exists largely in the

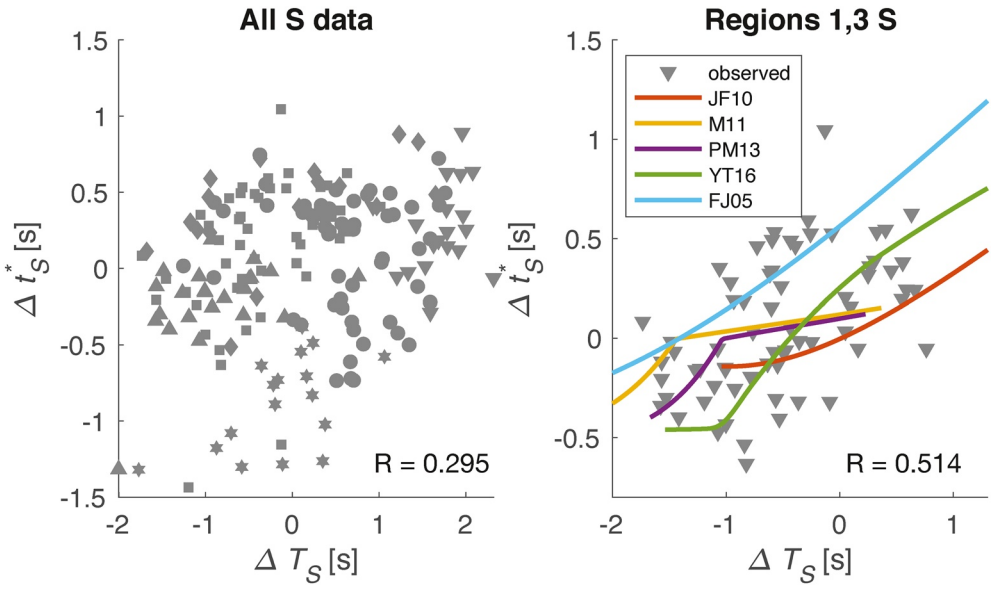

Figure 13. Comparison of ΔT_S and Δt_S^* measurements. (Left) all observations; symbols indicate regions from Figure 3. (Right) observations from just Regions 1 and 3, excluding sites in Bristol Bay Basin or Cook Inlet. Colored lines show predictions from laboratory-based models as labeled: JF10 (Jackson & Faul, 2010); M11 (McCarthy et al., 2011); PM13 (Priestley & McKenzie, 2013); YT16 (Yamauchi & Takei, 2016); FJ05 (Faul & Jackson, 2005). Calculations are made at 2.5 GPa, assuming 0.10 Hz signals, 5 mm grain size, temperatures ranging 1100°C–1500°C, and peridotite or olivine elasticity as described in these studies. Predictions assume signals are all generated at 30–220 km depth as discussed in Section 5.4. Each absolute prediction is converted to relative variations assuming a reference $Q_S = 109$ and $V_S = 4.45$ km/s corresponding to zero anomaly. To account for long-wavelength E-W variations in ΔT_S an arbitrary shift of 1.5 s is subtracted from its predictions.

upper 150–200 km. Velocity shows sensitivity to temperatures even far from the solidus, so ΔT has sensitivity to deeper structure in subduction zones.

Travel times and attenuation measurements also differ in their sensitivity to the presence of sedimentary basins. While low-velocity sediments have a first-order effect to delay ΔT measurements the teleseismic Δt^*measurements show no evidence of increased attenuation over basins, at the low frequencies of these signals. In fact, the Cook Inlet Basin shows the most negative $\Delta t^*$of any region from both the amplitude and phase spectra, suggesting the possibility of some sort of frequency-dependent phase delay mimicking negative differential attenuation here.

Attenuation is of the order $1000/Q_S \sim 8$–15 averaged over the upper 220 km of mantle. These measurements, dominated by frequencies of 0.2–0.5 Hz, are comparable to the global variations seen in surface-wave attenuation at these depths, and somewhat higher than inferred in the nearby Denali region from higher-frequency body waves. Some of that difference may reflect differences between the Cook Inlet and amagmatic Denali segments, as high-frequency measurements from other subduction zones are similar to the teleseismic measurements obtained here, and some frequency dependence may contribute. Uncertainties in the actual depth range and geographic area controlling the observed signals make direct comparisons difficult; a follow-on tomography study now underway should better evaluate the depth ambiguity.

Correlations between ΔT_P and ΔT_S, or between Δt_P^* and Δt_S^*, provide some evidence for the physical mechanisms giving rise to observed velocity and attenuation anomalies. Across the array, the measurements give $d(\ln V_S)/d(\ln V_P) \sim 1.46$ consistent with thermal processes and textural equilibrium in melt-rich areas. The attenuation measurements give dQ_P/dQ_S that require some bulk-modulus relaxation over the whole region, although the near-arc region are consistent with only shear attenuation.

Overall, the large-scale patterns seen here resemble those inferred from local-earthquake studies, suggesting that teleseismic measurements such as these provide useful complements to velocity imaging in subduction zones, particularly for the uppermost mantle.

Data Availability Statement

All waveform data are archived and openly available at the IRIS Data Management Center (www.iris.edu/ds), under station code YG (2016-18) for WVLF (Christensen & Abers, 2016; https://doi.org/10.7914/SN/YG_2016), ZE (2015-17) for SALMON (Tape et al., 2017; https://doi.org/10.7914/SN/ZE_2015), and TA for the Alaska Transportable Array (IRIS Transportable Array, 2003; https://doi.org/10.7914/SN/TA). The authors thank C. Tape for making SALMON data available prior to its release.

Acknowledgments
This research was supported by the National Science Foundation award EAR-1460291. New data collection for the WVLF experiment was supported by the IRIS-PASSCAL Instrument Center, which provided excellent logistical and technical support. We thank M. Bezada, an anonymous reviewer, and M. Bostock for insightful comments.

References

Abers, G. A., Fischer, K. M., Hirth, G., Wiens, D. A., Plank, T., Holtzman, B. K., et al. (2014). Reconciling mantle attenuation-temperature relationships from seismology, petrology and laboratory measurements. *Geochemistry, Geophysics, Geosystems*, *15*, 3521–3542. https://doi.org/10.1002/2014GC005444

Abers, G. A., van Keken, P. E., & Hacker, B. R. (2017). The cold and relatively dry nature of mantle forearcs in subduction zones. *Nature Geoscience*, *10*, 333–337. https://doi.org/10.1038/NGEO2922

Abers, G. A., van Keken, P. E., & Wilson, C. R. (2020). Deep decoupling in subduction zones: Observations and temperature limits. *Geosphere*, *16*, 1408–1424. https://doi.org/10.1130/GES02278.1

Anderson, D. L., & Minster, J. B. (1979). The frequency dependence of Q in the Earth and implications for mantle rheology and Chandler wobble. *Geophysical Journal of the Royal Astronomical Society*, *58*, 431–440. https://doi.org/10.1111/j.1365-246x.1979.tb01033.x

Berg, E. M., Lin, F., Allam, A., Schulte-Pelkum, V., Ward, K. M., & Shen, W. (2020). Shear velocity model of Alaska via joint inversion of Rayleigh wave ellipticity, phase velocities, and receiver functions across the Alaska transportable array. *Journal of Geophysical Research: Solid Earth*, *125*, e2019JB018582. https://doi.org/10.1029/2019jb018582

Bezada, M., Byrnes, J., & Eilon, Z. (2019). On the robustness of attenuation measurements on teleseismic P waves: Insights from micro-array analysis of the 2017 North Korean nuclear test. *Geophysical Journal International*, *218*, 573–585. https://doi.org/10.1093/gji/ggz169

Bezada, M. J. (2017). Insights into the lithospheric architecture of Iberia and Morocco from teleseismic body-wave attenuation. *Earth and Planetary Science Letters*, *478*, 14–26. https://doi.org/10.1016/j.epsl.2017.08.029

Brueseke, M. E., Benowitz, J. A., Trop, J. M., Davis, K. N., Berkelhammer, S. E., Layer, P. W., & Morter, B. K. (2019). The Alaska Wrangell Arc: ~30 Ma of subduction-related magmatism along a still active arc-transform junction. *Terra Nova*, *31*, 59–66. https://doi.org/10.1111/ter.12369

Bruns, T. R. (1983), Model for the origin of the Yakutat block, an accreting terrane in the northern Gulf of Alaska. *Geology*, *11*, 718–721.

Buurman, H., Nye, C. J., West, M. E., & Cameron, C. (2014). Regional controls on volcano seismicity along the Aleutian arc. *Geochemistry, Geophysics, Geosystems*, *15*, 1147–1163. https://doi.org/10.1002/2013GC005101

Christensen, D., & Abers, G. (2016). *Fate and consequences of Yakutat terrane subduction beneath eastern Alaska and the Wrangell Volcanic Field*. International Federation of Digital Seismograph Networks. https://doi.org/10.7914/SN/YG_2016

Christeson, G. L., Gulick, S. P. S., van Avendonk, H. J. A., Worthington, L. L., Reece, R. S., & Pavlis, T. L. (2010). The Yakutat terrane: Dramatic change in crustal thickness across the Transition fault, Alaska. *Geology*, *38*, 895–898. https://doi.org/10.1130/g31170.1

Dalton, C. A., Ekström, G., & Dziewonski, A. M. (2009). Global seismological shear velocity and attenuation: A comparison with experimental observations. *Earth and Planetary Science Letters*, *284*, 65–75. https://doi.org/10.1016/j.epsl.2009.04.009

Deng, Y., Byrnes, J. S., & Bezada, M. (2021). New insights into the heterogeneity of the lithosphere-asthenosphere system beneath South China from teleseismic body-wave attenuation. *Geophysical Research Letters*, *48*, e2020GL091654. https://doi.org/10.1029/2020GL091654

Dziewonski, A., Bloch, S., & Landisman, M. (1969). A technique for the analysis of transient seismic signals. *Bulletin of the Seismological Society of America*, *59*, 427–444.

Dziewonski, A. M., & Anderson, D. L. (1981). Preliminary reference Earth model. *Physics of the Earth and Planetary Interiors*, *25*, 297–356. https://doi.org/10.1016/0031-9201(81)90046-7

Eberhart-Phillips, D., Christensen, D. H., Brocher, T. M., Hansen, R., Ruppert, N. A., Haueussler, P. J., & Abers, G. A. (2006). Imaging the transition from Aleutian subduction to Yakutat collision in central Alaska, with local earthquakes and active source data. *Journal of Geophysical Research*, *111*, B11303. https://doi.org/10.1029/2005JB004240

Eilon, Z. C. (2016). *New constraints on extensional environments through analysis of teleseisms (PhD)* (p. 217). Columbia University.

Eilon, Z. C., & Abers, G. A. (2017). High seismic attenuation at a mid-ocean ridge reveals the distribution of deep melt. *Science Advances*, *3*, e1602829. https://doi.org/10.1126/sciadv.1602829

Elliott, J., & Freymueller, J. T. (2020). A block model of present-day kinematics of Alaska and Western Canada. *Journal of Geophysical Research: Solid Earth*, *125*, e2019JB018378. https://do10.1130/10.1029/2019JB018378

Faul, U. H., FitzGerald, J. D., & Jackson, I. (2004). Shear wave attenuation and dispersion in melt-bearing olivine polycrystals: 2. Microstructural interpretation and seismological implications. *Journal of Geophysical Research*, *109*, B06202. https://doi.org/10.1029/2003JB002407

Faul, U. H., & Jackson, I. (2005). The seismological signature of temperature and grain size variations in the upper mantle: Earth Planet. *Science Letter*, *234*, 119–134. https://doi.org/10.1016/j.epsl.2005.02.008

Ferris, A., Abers, G. A., Christensen, D. H., & Veenstra, E. (2003). High resolution image of the subducted Pacific (?) plate beneath central Alaska, 50–150 km depth. *Earth and Planetary Science Letters*, *214*, 575–588. https://doi.org/10.1016/s0012-821x(03)00403-5

Finzel, E., Flesch, L., & Ridgway, K. (2011). Kinematics of a diffuse North America–Pacific–Bering plate boundary in Alaska and western Canada. *Geology*, *39*, 835–838. https://doi.org/10.1130/g32271.1

Frost, D. A., Romanowicz, B., & Roecker, S. (2020). Upper mantle slab under Alaska: Contribution to anomalous core-phase observations on south-Sandwich to Alaska paths. *Physics of the Earth and Planetary Interiors*, *299*, 106427. https://doi.org/10.1016/j.pepi.2020.106427

Gou, T., Zhao, D., Huang, Z., & Wang, L. (2019). Aseismic deep slab and mantle flow beneath Alaska: Insight from anisotropic tomography. *Journal of Geophysical Research: Solid Earth*, *124*, 1700–1724. https://doi.org/10.1029/2018JB016639

Hammond, W. C., & Humphreys, E. D. (2000). Upper mantle seismic wave velocity: Effects of realistic partial melt geometries. *Journal of Geophysical Research*, *105*(10), 975–986. https://doi.org/10.1029/2000jb900041

Hirschmann, M. M. (2006). Water, melting, and the deep earth H_2O cycle. *Annual Review of Earth and Planetary Sciences*, *34*, 629–653. https://doi.org/10.1146/annurev.earth.34.031405.125211

IRIS Transportable Array. (2003). *US Array Transportable Array*. International Federation of Digital Seismograph Networks. https://doi.org/10.7914/SN/TA

Jackson, I., & Faul, U. H., 2010, Grainsize-sensitive viscoelastic relaxation in olivine: Toward a robust laboratory-based model for seismological application. *Physics of the Earth and Planetary Interiors*, *183*, 151–163. https://doi.org/10.1016/j.pepi.2010.09.005

Jiang, C., Schmandt, B., Ward, K. M., Lin, F., & Worthington, L. L. (2018). Upper mantle seismic structure of Alaska from Rayleigh and S wave tomography. *Geophysical Research Letters*, *45*, 10–350. https://doi.org/10.1029/2018gl079406

Karato, S. (1993). Importance of anelasticity in the interpretation of seismic tomography. *Geophysical Research Letters*, *20*, 1623–1626. https://doi.org/10.1029/93gl01767

Karato, S. (2003). Mapping water content in the upper mantle. In Eiler, J. M. (Ed.), *Inside the subduction factory, geophysical monograph series 138* (pp. 135–152). Washington: American Geophysical Union. https://doi.org/10.1029/138gm08

Kissling, E., & Lahr, J. C. (1991). Tomographic image of the Pacific slab under southern Alaska. *Eclogae Geologicae Helvetiae*, *84*, 297–315.

Lee, C.-T. A., Luffi, P., Plank, T., Dalton, H., & Leeman, W. P. (2009). Constraints on the depths and temperatures of basaltic magma generation on Earth and other terrestrial planets using new thermobarometers for mafic magmas. *Earth and Planetary Science Letters*, *279*, 20–33. https://doi.org/10.1016/j.epsl.2008.12.020

Li, J., Abers, G. A., Kim, Y. H., & Christensen, D. (2013). Alaska Megathrust 1: Seismicity 43 years after the great 1964 Alaska megathrust earthquake. *Journal of Geophysical Research*, *118*, 4861–4871. https://doi.org/10.1002/jgrb.5035810.1002/jgrb.50358

Mann, M. E., & Abers, G. A. (2020). First-order mantle subduction-zone structure effects on ground motion: The 2016 M w 7.1 Iniskin and 2018 M w 7.1 Anchorage earthquakes. *Seismological Research Letters*, *91*, 85–93. https://doi.org/10.1785/0220190197

Martin-Short, R., Allen, R., Bastow, I. D., Porritt, R. W., & Miller, M. S. (2018). Seismic imaging of the Alaska subduction zone: Implications for slab geometry and volcanism. *Geochemistry, Geophysics, Geosystems*, *19*, 4541–4560.

Martin-Short, R., Allen, R. M., & Bastow, I. D. (2016). Subduction geometry beneath south central Alaska and its relationship to volcanism. *Geophysical Research Letters*, *43*, 9509–9517. https://doi.org/10.1002/2016GL070580

McCarthy, C., Takei, Y., & Hiraga, T. (2011). Experimental study of attenuation and dispersion over a broad frequency range: 2. The universal scaling of polycrystalline materials. *Journal of Geophysical Research*, *116*, B09207. https://doi.org/10.1029/2011JB008384

McPherson, A., Christensen, D., Abers, G., & Tape, C. (2020). Shear wave splitting and mantle flow beneath Alaska. *Journal of Geophysical Research: Solid Earth*, *125*, e2019JB018329. https://doi.org/10.1029/2019jb018329

Miller, M. S., O'Driscoll, L. J., Porritt, R. W., & Roeske, S. M. (2018). Multiscale crustal architecture of Alaska inferred from P receiver functions. *Lithosphere*, *10*(2), 267–278. https://doi.org/10.1130/L701.1

Moschetti, M. P., Thompson, E. M., Rekoske, J., Hearne, M. G., Powers, P. M., McNamara, D. E., & Tape, C. (2020). Ground-motion amplification in Cook Inlet region, Alaska, from intermediate-depth earthquakes, Including the 2018 M w 7.1 Anchorage Earthquake. *Seismological Research Letters*, *91*, 142–152. https://doi.org/10.1785/0220190179

Müller, T. M., Gurevich, B., & Lebedev, M. (2010). Seismic wave attenuation and dispersion resulting from wave-induced flow in porous rocks—A review. *Geophysics*, *75*, 75A147–75A164. https://doi.org/10.1190/1.3463417

Nayak, A., Eberhart-Phillips, D., Ruppert, N. A., Fang, H., Moore, M. M., Tape, C., et al. (2020). 3D seismic velocity models for Alaska from joint tomographic inversion of body-wave and surface-wave data, *Seismological Society of America*, *91*, 3106–3119. https://doi.org/10.1785/0220200214

Nye, C., Begét, J. E., Layer, P. W., Mangan, M. T., McConnell, V. S., McGimsey, R. G., et al. (2018). *Geochemistry of some quaternary lavas from the Aleutian arc and Mt. Wrangell: Raw data file RDF 2018-1: State of Alaska*. Department of Natural Resources, Division of Geological & Geophysical Surveys. https://doi.org/10.14509/29843

Page, R. A., Stephens, C. D., & Lahr, J. C. (1989). Seismicity of the Wrangell and Aleutian Wadati-Benioff zones and the North America plate along the Trans-Alaska crustal transect, Chugach Mountains and Copper River basin, southern Alaska. *Journal of Geophysical Research*, *94*, 16059–16082. https://doi.org/10.1029/jb094ib11p16059

Pavlis, T. L., Picornell, C., Serpa, L., Bruhn, R. L., & Plafker, G. (2004). Tectonic processes during oblique collision: Insights from the St. Elias orogen, northern North American Cordillera. *Tectonics*, *23*, TC3001. https://doi.org/10.1029/2003TC001557

Plafker, G., & Berg, H. C. (1994). Overview of the geology and tectonic evolution of Alaska. In Plafker (Ed.), *The geology of Alaska, the geology of North America, G-1, boulder, Colorado* (pp. 989–1021). Geological Society of America.

Pozgay, S. H., Wiens, D. A., Conder, J. A., Shiobara, H., & Sugioka, H. (2009). Seismic attenuation tomography of the Mariana subduction system: Implications for thermal structure, volatile distribution, and slow spreading dynamics. *Geochemistry, Geophysics, Geosystems*, *10*, Q04X05. https://doi.org/10.1029/2008GC002313

Preece, S. J., & Hart, W. K. (2004). Geochemical variations in the < 5 Ma Wrangell Volcanic Field, Alaska: Implications for the magmatic and tectonic development of a complex continental arc system. In *8th international symposium on deep seismic profiling of the continents and their margins* (Vol. 392, pp. 165–191). https://doi.org/10.1016/j.tecto.2004.04.011

Priestley, K., & McKenzie, D. (2013). The relationship between shear wave velocity, temperature, attenuation and viscosity in the shallow part of the mantle. *Earth and Planetary Science Letter*, *381*, 78–91. https://doi.org/10.1016/j.epsl.2013.08.022

Ratchkovski, N. A., & Hansen, R. A. (2002). New constraints on tectonics of interior Alaska: Earthquake locations, source mechanisms, and stress regime. *Bulletin of the Seismological Society of America*, *92*, 998–1014. https://doi.org/10.1785/0120010182

Richter, D., Smith, J. G., Lanphere, M., Dalrymple, G., Reed, B., & Shew, N. (1990). Age and progression of volcanism, Wrangell volcanic field, Alaska. *Bulletin of Volcanology*, *53*, 29–44.

Roth, E. G., Wiens, D. A., Dorman, L. M., Hildebrand, J., & Webb, S. C. (1999). Seismic attenuation tomography of the Tonga back-arc region using phase pair methods. *Journal of Geophysical Research*, *104*, 4795–4809. https://doi.org/10.1029/1998jb900052

Ruppert, N. A., & West, M. E. (2020). The Impact of US Array on Earthquake Monitoring in Alaska. *Seismological Research Letters*, *91*, 601–610. https://doi.org/10.1785/0220190227

Rychert, C. A., Fischer, K. M., Abers, G. A., Plank, T., Syracuse, E., Protti, J. M., et al. (2008). Strong along-arc variations in attenuation in the mantle wedge beneath Costa Rica and Nicaragua. *Geochemistry, Geophysics, Geosystem*, *9*, Q10S10. https://doi.org/10.1029/2008gc002040

Shellenbaum, D. P., Gregersen, L. S., & Delaney, P. R. (2010). *Top Mesozoic unconformity depth map of the Cook Inlet basin*. Alaska: Alaska Division of Geological and Geophysical Surveys Report of Investigations.

Smith, K., & Tape, C. (2020). Seismic response of Cook Inlet sedimentary basin. *Southern Alaska: Seismological Research Letters*, *91*, 33–55. https://doi.org/10.1785/0220190205

Soto Castaneda, R. A. (2020). Teleseismic P and S wave attenuation constraints on temperature and melt. In *Of the upper mantle in the Alaska subduction zone* (MS Thesis) (p. 112). Cornell University.

Stachnik, J. C., Abers, G. A., & Christensen, D. (2004). Seismic attenuation and mantle wedge temperatures in the Alaska subduction zone. *Journal of Geophysical Research*, *109*, B10304. https://doi.org/10.1029/2004JB003018

Takei, Y. (2002). Effect of pore geometry on *Vp*/*Vs*: From equilibrium geometry to crack. *Journal of Geophysical Research*, *107*. https://doi.org/10.1029/2001JB000522

Takei, Y. (2017). Effects of partial melting on seismic velocity and attenuation: A new insight from experiments. *Annual Review of Earth and Planetary Sciences*, *45*, 447–470. https://doi.org/10.1146/annurev-earth-063016-015820

Tape, C., Christensen, D., Moore-Driskell, M. M., Sweet, J., & Smith, K. (2017). Southern Alaska Lithosphere and Mantle Observation Network (SALMON): A seismic experiment covering the active arc by road, boat, plane, and helicopter. *Seismological Research Letters*, *88*, 1185–1202. https://doi.org/10.1785/0220160229

Trop, J. M., & Ridgway, K. D. (2007). Mesozoic and Cenozoic tectonic growth of southern Alaska: A sedimentary basin perspective. In Ridgway, K. D., Trop, J. M., Glen, J., & O'Neill, J. (Eds), *Tectonic growth of a collisional continental margin: Crustal evolution of Southern Alaska*. (Vol. 431), (pp. 55–94). Geological Society of America. https://doi.org/10.1130/2007.2431(04)

Van Decar, J. C., & Crosson, R. S. (1990). Determination of teleseismic relative phase arrival times using multi-channel cross-correlation and least squares. *Bulletin of the Seismological Society of America*, *80*, 150–159.

Van Stiphout, A., Cottaar, S., & Deuss, A. (2019). Receiver function mapping of mantle transition zone discontinuities beneath Alaska using scaled 3-D velocity corrections. *Geophysical Journal International*, *219*, 1432–1446. https://doi.org/10.1093/gji/ggz360

Wang, Y., & Tape, C. (2014). Seismic velocity structure and anisotropy of the Alaska subduction zone based on surface wave tomography. *Journal of Geophysical Research: Solid Earth*, *119*, 8845–8865. https://doi.org/10.1002/2014jb011438

Ward, K. M. (2015). Ambient noise tomography across the southern Alaskan cordillera. *Geophysical Research Letters*, *42*, 3218–3227. https://doi.org/10.1002/2015gl063613

Wei, S. S., & Wiens, D. A. (2018). P-wave attenuation structure of the Lau back-arc basin and implications for mantle wedge processes. *Earth and Planetary Science Letters*, *502*, 187–199. https://doi.org/10.1016/j.epsl.2018.09.005

Wei, S. S., & Wiens, D. A. (2020). High bulk and shear attenuation due to partial melt in the Tonga-Lau back-arc mantle. *Journal of Geophysical Research: Solid Earth*, *125*, e2019JB017527. https://doi.org/10.1029/2019JB017527

Worthington, L. L., Van Avendonk, H. J. A., Gulick, S. P. S., Christeson, G. L., & Pavlis, T. L. (2012). Crustal structure of the Yakutat terrane and the evolution of subduction and collision in southern Alaska. *Journal of Geophysical Research*, *117*, B01102. https://doi.org/10.1029/2011jb008493

Yamauchi, H., & Takei, Y. (2016). Polycrystal anelasticity at near-solidus temperatures. *Journal of Geophysical Research*, *121*, 7790–7820. https://doi.org/10.1002/2016jb013316

Zhao, D., Christensen, D. H., & Pulpan, H. (1995). Tomographic imaging of the Alaska subduction zone. *Journal of Geophysical Research*, *100*, 6487–6504. https://doi.org/10.1029/95jb00046